BENEMÉRITA UNIVERSIDAD AUTÓNOMA DE PUEBLA

INSTITUTO DE FÍSICA “LUIS RIVERA TERRAZAS”

“ELECTRONIC STATES AND TRANSPORT IN PROXIMITY OF BIDIMENSIONAL MATERIALS”

TESIS

QUE PARA OBTENER EL GRADO DE

MAESTRO EN CIENCIAS
(FÍSICA)

PRESENTA:
NOHORA ALEJANDRA HERNÁNDEZ CEPEDA

ASESOR(ES):
Dra. LILIA MEZA MONTES
Dr. SERGIO E. ULLOA

No. de CVU: 928270

JUNIO DE 2020

Universidad Autónoma de Puebla
Instituto de Física "Luis Rivera Terrazas"

Electronic states and transport in proximity of bidimensional materials

Tesis presentada por

Nohora Alejandra Hernández Cepeda

para obtener el grado de

Maestra en Ciencias
(Física)

Dirigida por
Dra. Lilia Meza Montes **Dr. Sergio E. Ulloa**

Puebla, México
Junio 2020

Acknowledgements

I would like to thank my advisors, Dr. Lilia Meza and Dr. Sergio Ulloa, for their guidance through each stage of the research and the writing of the thesis, as well as for inspiring my interest in the study of bidimensional materials. Finally, I acknowledge to Instituto de Física "Luis Rivera Terrazas" and the financial support of CONACyT.

Resumen

En la espintrónica y sus aplicaciones, la manipulación del espín de los portadores es fundamental. Los materiales bidimensionales ofrecen una gran gama de posibilidades para lograr este objetivo. Así, en este trabajo, se estudiaron los estados electrónicos y el transporte en el grafeno cuando este se encuentra en proximidad con una nanocinta de dicalcogenuros de metales de transición (TMD), y está bajo la acción de un campo magnético aplicado. Para ello, se utilizó el modelo de Hamiltoniano efectivo, cuyos valores y vectores propios dan lugar a la estructura de bandas de energía y las texturas de espín, respectivamente. Los resultados muestran que existen dos regímenes en la heteroestructura de grafeno y TMD (hG-TMD), a saber, aquel en el que las bandas presentan inversión de espín (*banda invertida*), y donde las bandas tienen estados de espín con la misma orientación (*bandgap directo*). Se encontró que la probabilidad de que un electrón sea transmitido o reflejado a través de un sistema compuesto por grafeno y una cinta de hG-TMD con *spin-down* es mayor conforme esta probabilidad con *spin-up* decrece, y es óptima en el régimen de *bandgap directo.* El régimen está determinado por la intensidad de la interacción espín-órbita. Adicionalmente, cuando se aplica un campo magnético en el plano de hG-TMD, la simetría alrededor del punto K de la estructura de bandas de energía y texturas de espín se preserva a lo largo de esta dirección, de lo contrario, se rompe; a su vez, las probabilidades de modificar el espín, cuando el electrón es transmitido o reflejado, incrementan conforme aumenta la intensidad del campo aplicado. Por último, se obtienen niveles de Landau espín-degenerados para un campo Zeeman y en ausencia de Rashba. De acuerdo con los resultados, se evidencia que el control del espín electrónico es posible en el grafeno al incrementar el efecto espín-órbita mediante el efecto de proximidad inducido por TMD. Los parámetros de control son la intensidad del efecto, el ancho de la cinta de TMD y el campo magnético.

Abstract

The manipulation of carriers' spin is fundamental in spintronics and its applications. Two-dimensional materials offer many possibilities to achieve this target. Thus, in this work, we study the electronic states and transport in graphene in proximity to a nanoribbon of transition metal dichalcogenides (TMD), and under the action of an applied magnetic field. For this purpose, the effective Hamiltonian model is used in such a way that eigenvalues and eigenvectors give rise to the energy band structure and the spin textures, respectively. The results show that two regimes exist in the heterostructure of graphene and TMD (hG-TMD): one in which the bands have inverted curvature (*inverted band*), and another where the bands have states of regular curvature (*direct bandgap*), depending on the spin-orbit interaction. It was found that the probability of an electron with spin-down being transmitted or reflected through a system composed of graphene and TMD ribbon increases as the one with spin-up decreases, and is optimal in the regime of *direct bandgap.* Furthermore, when a magnetic field is applied along the hG-TMD plane, the symmetry of the energy band structure and spin textures around the K point is preserved along the field direction, while breaking otherwise. As the intensity of the applied magnetic field increases, the probability of flipping spin when the electron is transmitted or reflected, increases. Finally, spin-degenerated Landau levels were obtained for a Zeeman field in the absence of Rashba coupling. In accordance to the results, the electronic spin control is possible in graphene because of the increase of the spin-orbit effect due to the proximity of TMD. The control parameters are the intensity of the SOC effect, the TMD ribbon width, and the magnetic field.

Participation in events

- Electronic states and transport in graphene-TMD heterostructures, Nohora Hernández Cepeda, L. Meza-Montes, Sergio E. Ulloa, March Meeting, Denver, Colorado, USA (2020). Link: http://meetings.aps.org/Meeting/MAR20/Session/F53.14

Contents

Introduction

This work considers the electronic states and electron transport in graphene when this is in proximity to a semiconducting transition metal dichalcogenides (TMD) substrate. We have analyzed the changes introduced when a magnetic field is applied along different directions. To accomplish this study, an effective Hamiltonian model has been used, as their eigenstates allow we to obtain the energy band structures, spin textures, and transmission and reflection coefficients associated to an electron moving through the system.

The study of such heterostructures is relevant for the investigation of a variety of properties not present in their bulk or pristine counterparts. Indeed, the proximity between graphene and TMD allows the first one to experience an enhancement of its spin-orbit-coupling, proportionally to the TMD intrinsic spin-orbit coupling (SOC). This behavior suggests to consider the hG-TMD as a suitable system for spintronics. Thus, this document has been elaborated in such a way that enables us to comprehend, with the help of analytical and numerical work, how the graphene is affected by the presence of TMD and magnetic fields.

In the first chapter, the theoretical and experimental works that have previously described how the proximity effect of TMD on graphene arises are presented. Indeed, this effect is modeled through the low-energy effective Hamiltonian. Its eigenstates reflect the changes introduced by an intrinsic SOC, Rashba SOC, main introduced gap Δ induced by an effective staggered potential, and an external magnetic field.

The second chapter is divided into two sections: first of all, the theoretical model is given in detail. The explicit forms of the effective Hamiltonian, the magnetic field-spin interaction Hamiltonian and the expected value of spin are presented to discuss the general characteristics of the model and resulting eigenstates. In second place, results for the energy band structures and spin textures are displayed for *Strong* and *Weak SOC* regimes, as well as the changes introduced by the magnetic field, applied on the plane and along the z direction.

In the third chapter, we present the systems through which the electronic transport is analyzed, as well as the electron's wave functions, the continuity conditions, and the transfer matrix for the corresponding cases (*Strong/Weak SOC* regime with/without magnetic field). Taking this into account, we calculate the spin-dependent transmission and reflection probabilities for an electron moving through a graphene-TMD ribbon on top of it, which are also modulated by a magnetic field on the plane.

Finally, the results obtained in the two previous sections are summarized. To conclude, further perspectives that will guide future investigations are proposed.

Chapter 1

Graphene and TMD heterostructures

1.1 2D materials: the case of Graphene and TMD

Since the discovery of graphene, a semimetal, the family of two dimensional materials has grown. Finding other materials with different properties has been possible. For example, insulators, semiconductors, semimetals, and metals have been discovered in their 2D form. One of the most important features of these materials is that they behave differently from their bulk counterpart [1].

Energy band structure of a 2D-material can be modified with the variation of the number of atomic layers, intercalation, interlayer twist, or by placing this material in proximity to different substrates [2]. From this perspective, few-atoms-thick materials also offer a new possibility: to develop heterostructures with a variety of properties. In this sense, it is possible to make sandwich structures composed of two, three, or a variety of layers of such materials. Strong covalent bonds are sufficient to make the crystals stable across the plane, and van der Waals forces, which are relatively weak, keeping the stack together [3].

Due to the different electronic structures and properties of the materials, it is feasible to put together as many different few-layers crystals as possible in order to create a stack with the desired properties, which are fragile or not present in their original version [4].

1.1.1 Graphene

Graphene was the first 2D material accessible to the scientific community. This hexagonal periodic structure has been intensively studied during the last years because of its properties. For example, the electron mobility at room temperature is ultra-high as well as its thermal conductivity. Also, it is totally impermeable to any gases and has a very large Young's modulus, which gives interesting mechanical and elastic properties [5].

Despite of these described exceptional properties, there are other features, like very small intrinsic spin-orbit coupling (SOC) and graphene's semimetal character, limiting its practical applications [2]. Researchers have found that it is possible to enhance these properties when graphene interacts with other 2D-crystal (like transition metal dichalcogenides TMD) in order to build van der Waals heterostructures.

It would be important to point out some concepts of graphene as its crystal and electronic structures.

Crystal structure of graphene

Graphene is a honeycomb periodic structure. This can be seen as a triangular lattice composed of two atoms A and B per primitive cell. There are some important high symmetry points like Γ, at the center of the first Brillouin zone (FBZ), and K and K' points in the corners, which are not equivalent [6]. The valence and conduction bands of the band energy structure of graphene coincide at these points, which are named Dirac points.

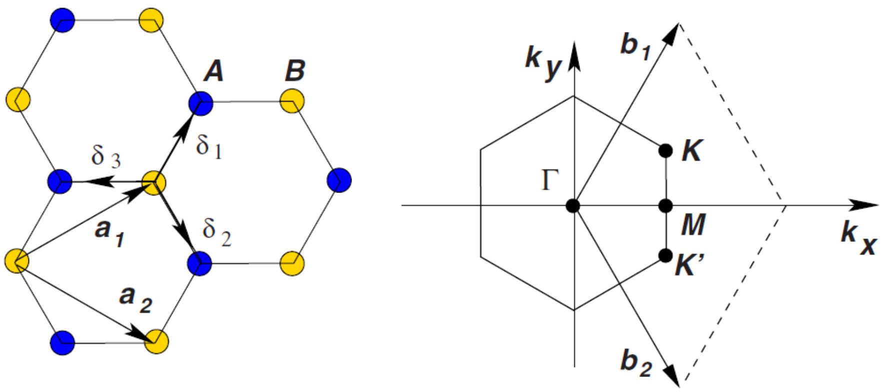

Figure 1.1: Graphene hexagonal lattice and its First Brillouin zone [7].

According to the figure 1.1, we present all the vectors involved in the description of graphene in the hexagonal lattice and in its First Brillouin zone [7]. The left side of the structure can be described in terms of the lattice vectors:

$$\mathbf{a_1} = \frac{a}{2}(3, \sqrt{3}), \mathbf{a_2} = \frac{a}{2}(3, -\sqrt{3}). \tag{1.1}$$

where $a \approx 1.42\,\text{Å}$ is the distance between two atoms of carbon. On the other hand, in the reciprocal-lattice, vectors can be written as:

$$\mathbf{b_1} = \frac{2\pi}{3a}(1, \sqrt{3}), \mathbf{b_2} = \frac{2\pi}{3a}(1, -\sqrt{3}). \tag{1.2}$$

Taking into account these definitions, it is possible to describe the three nearest neighbor vectors in real space as follows:

$$\delta_{\mathbf{1}} = \frac{a}{2}(1, \sqrt{3}), \delta_{\mathbf{2}} = \frac{a}{2}(1, -\sqrt{3}), \delta_{\mathbf{3}} = -a(1, 0). \tag{1.3}$$

Besides, the points K and K' in the momentum space are given by:

$$\mathbf{K} = (\frac{2\pi}{3a}, \frac{2\pi}{3\sqrt{3}a}), \mathbf{K'} = (\frac{2\pi}{3a}, -\frac{2\pi}{3\sqrt{3}a}), \tag{1.4}$$

Electronic configuration

The electronic structure of a carbon atom is $(1s)^2(2s)^2(2p)^2$, which means four electrons are in the valence band. Hybridization can precisely occur in orbitals 2s and 2p. In the case of graphene, sp^2 hybridization takes place: 2s orbital is mixed with two ($2p_x$ and $2p_y$) of the three available 2p orbitals, leaving unaffected one p orbital ($2p_z$). The tendency is for sp^2 orbitals to organize themselves in a trigonal planar structure with σ bonds between carbon atoms, which are separated by 1.42Å [7]. The unaffected $2p_z$ orbital is perpendicular to the planar structure. It is useful because carbon atoms can bond with neighbors atoms through π bonds.

1.1.2 Transition metal dichalcogenides

Transition metal dichalcogenides (TMD's) are semiconductor layered materials of the form MX_2, which implies that a transition metal (M) layer is sandwiched between two layers of chalcogens (X). Examples include molybdenum disulfide (MoS_2), molybdenum diselenide ($MoSe_2$), tungsten disulfide (WS_2), and tungsten diselenide (WSe_2) [8]. Such

2D materials have a hexagonal lattice, whose FBZ is also hexagonal and the band has two nonequivalent points: K and K' (high symmetry points) [9].

TMD's can transit from indirect bandgap in their 3D form to direct bandgap as they scaled down to monolayer form. Such characteristic is relevant in practical terms because materials like MoS_2 could be used in light-emitting diodes, photodetectors, or solar cells [10]. Furthermore, these materials have a strong SOC due to d orbitals of the heavy metal atoms, that means SOC increases when metal atomic number augments [11], [2]. This feature finds applications in spintronics.

To combine the characteristics of graphene and semiconductor TMD's, as well as to mitigate the unwanted properties, researchers have investigated, both theoretically and experimentally, how graphene and TMD can be combined in a van der Waals heterostructure. This heterostructure has been studied with graphene/MoS_2 and graphene/WS_2. It is important to mention that these structures do not have commensurable lattices, which implies that properties are likely to be tuned by manipulating various factors such as interlayer twist, number of layers, interlayer separation., etc. [2].

It has been demonstrated experimentally that deposition of graphene on metallic substrates enhances SOC of the first one: particularly, the growth of graphene on MoS_2 and WS_2 [12]. Increasing SOC in graphene is due to the interaction between these materials. Thus, the electric field produced by TMD charges modifies SOC of graphene as this experiences a higher effective electric field due to d orbitals of metal atoms.

Additionally, the proximity of TMD induces a bandgap in the energy structure of graphene at the Dirac points and its electronic properties remain. This is especially interesting because the graphene-TMD heterostructure (hG-TMD) preserves the large mobility of electrons in graphene, which is useful for transport measurements [13].

Taking into account the above-mentioned points, we are going to discuss some experimental configurations that have found this increment of graphene's SOC in proximity with TMD, as well as its usefulness.

In the first place, a device composed of monolayer graphene and few-layers of tungsten disulfide (WS_2) was experimentally created to study SOC in graphene due to TMD proximity (see figure 1.2a). This is particularly relevant because it allows room temperature transport ballistic charge and gate-tunability, which is ideal for the spin field-effect transistor. Avsar *et al.* [14] demonstrated that graphene/WS_2 heterostructure keeps high mobilities and SOC of graphene increases up to 17meV, without modification of graphene structure. Therefore, this SOC, due to proximity, may yield spin Hall effect even at room temperature.

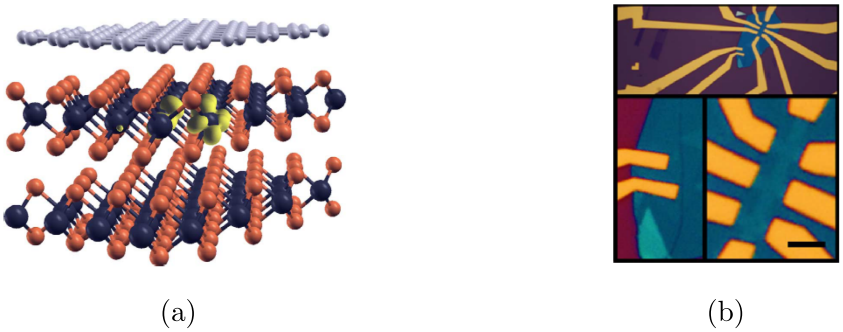
(a)

(b)

Figure 1.2: Device features. a) Schematic representation of a multilayer graphene/WS_2. W, S and C atoms are represented by dark grey, orange and light-grey spheres, respectively.; b) Optical image of a typical final device. Darker blue color represents the WS_2 substrate and lighter blue shows where graphene is located on substrate; yellow bars are contacts. Thus, this device has multiple Hall bar junctions on G/WS_2 heterostructure. Taken from [14].

Secondly, Island *et al.* [15] have studied the proximity effect experimentally in 2D crystals. They built interfaces of tungsten diselenide (WSe_2) and BLG (bilayer graphene), then, add hBN and graphite at each end of the structure (see figure 1.3). This system allows them to find that proximity effects make topological insulators possible as well as correlated quantum phases under the regime of intense SOC in graphene-based heterostructures.

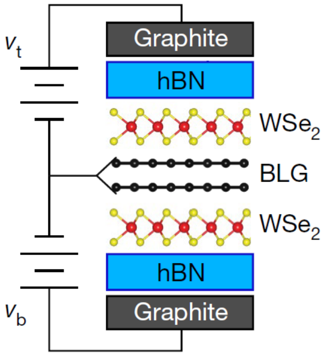

Figure 1.3: Device schematic. Taken from [15].

1.2 Effective Hamiltonian

In this section, we are going to discuss the theoretical model that has been used to describe the proximity effect in G-TMD structure. Therefore, an effective Hamiltonian model is proposed in order to detail the changes suffered by graphene energy band structure due to its proximity to TMD.

The effective Hamiltonian model takes into account the preserved and broken symmetries. The Hamiltonian contains broken inversion symmetry (P symmetry), as a result of the proximity of the TMD monolayer to graphene, as well as preservation of time-reversal symmetry [12]. Moreover, this Hamiltonian is built around K and K' points of graphene in the Brillouin zone, which implies that it is focusing only on the low-energy region of the energy band structure (a few meV around K point) [16].

It should also be highlighted that the model of effective Hamiltonian has allowed to find that hG-TMD produces an enhancement of SOC of graphene proportional to the intrinsic SOC of TMD [12]. Thus, the following terms describe different terms of perturbation that induce gaps in the graphene energy band structure.

The total Hamiltonian is written down as:

$$H_{eff} = H_0 + H_\Delta + H_{S1} + H_{S2} + H_R \tag{1.5}$$

and the following terms describe the different perturbations to the pristine graphene H_0, resulting in gaps in graphene band structure and other changes.

$$\begin{aligned} H_0 &= \hbar v_f(\tau_z s_0 \sigma_x k_x + \tau_0 s_0 \sigma_y k_y), \\ H_\Delta &= \Delta \tau_0 s_0 \sigma_z, \\ H_{S_1} &= S_1 \tau_z s_z \sigma_z, \\ H_{S_2} &= S_2 \tau_z s_z \sigma_{0,} \\ H_R &= R(\tau_z s_y \sigma_x - \tau_0 s_x \sigma_y). \end{aligned} \tag{1.6}$$

where v_f is the Fermi velocity ($\simeq 10^6 \frac{m}{s}$), Δ, S_1, S_2 and R are constants to be found by utilizing tight-binding calculation or first principles methods based on density functional theory (DFT). Consequently, the parameter values are related to the specific features of hG-TMD.

Each Hamiltonian is given in terms of 2x2 Pauli matrices, σ_i, τ_i and s_i (*i=0 represents the unit matrix*), which act on different degrees of freedom. Thus, σ_i operates on sublattices A and B; τ_i acts on K and K' in valley space; and s_i operates on the spin.

H_0 is the Hamiltonian for pristine graphene. This describes gapless states with the dispersion relation $E_G = \hbar v_f |k|$ [17]. The first considered term that could open a gap is H_Δ, which is proportional to σ_z. Indeed σ_z is odd under parity, which implies that the new gap on graphene is due to the inequivalence of A and B sublattices under exchange: there is an asymmetry because of the proximity of graphene to TMD monolayer.

H_{S_1} is the intrinsic SOC that preserves spatial symmetries of the honeycomb lattice. Furthermore, it could open a gap in the heterostructure differentiating valleys K and K' [12]. H_{S_2} is the diagonal SOC that represents a break in the particle-hole symmetry [2]. Finally, H_R is Rashba SOC owed to the presence of TMD (substrate) in proximity to graphene. As a consequence of this, lateral mirror symmetry is broken. The Rashba term mixes spin-up and spin-down [13]: this is essential to the understanding of the energy band structure of hG-TMD, which will be shown in the next chapter.

The basis in which this Hamiltonian is written is:

$$\Psi_{K,K'} = \begin{pmatrix} \psi_{A\uparrow K} \\ \psi_{B\uparrow K} \\ \psi_{A\downarrow K} \\ \psi_{B\downarrow K} \\ \psi_{A\uparrow K'} \\ \psi_{B\uparrow K'} \\ \psi_{A\downarrow K'} \\ \psi_{B\downarrow K'} \end{pmatrix} \tag{1.7}$$

where the elements of this basis represent the electron wave function in a particular sublattice A or B, with spin-up or spin-down and located on valley K or K'. Thus, the basis separates electron wave function in the K-valley in the first four components, and the latter four are associated with K'-valley. This is due to effective Hamiltonian takes into account the decoupling of K and K' valleys.

1.3 External perpendicular magnetic field

It has been said that the magnetic field is a source of broken symmetry, particularly the time-reversal symmetry. For this reason, another way in which we can introduce gaps in the energy band structure of graphene, besides the previously-mentioned is by applying a magnetic field coupled with spin, that is a Zeeman field. In principle, it is possible to place the magnetic field along whatever direction, but only when this is perpendicular to the structure, the dynamics of electronic states change.

From this point of view, we are going to review some effective Hamiltonian that describes graphene under intense SOC, with an extra Zeeman field term.

Firstly, research has been done on the electronic properties of a graphene monolayer under the action of high SOC intrinsic and Rashba, as well as under piecewise constant electrostatic potentials or magnetic field coupled with spin and strain-induced vector potentials [18]. The effective Hamiltonian that describes this system is given by:

$$\begin{aligned} H = v_f[\tau_z s_0 \sigma_x (p_x + \frac{e}{c}(A_x + a_x)) + \tau_0 s_0 \sigma_y (p_y + \frac{e}{c} a_y)] \\ + V + b s_z + R(\tau_z s_y \sigma_x - \tau_0 s_x \sigma_y) + S_1 \tau_z s_z \sigma_z. \end{aligned} \tag{1.8}$$

The vector potential is $\mathbf{A} = (-B(y - c_0), 0, 0)$, this implies that the magnetic field is along the z direction $B_z = B$. Hamiltonian commutes with p_x (then this momentum conserved) while p_y does not commute. In this case, the system is homogeneous along the x direction and constant piecewise in y. The coefficient $b = \mu_B B$ is the Zeeman coupling, where μ_B is the Bohr magneton and use $g_s = 2$. S_1 and R are intrinsic and Rashba SOC terms,as before, while a_i are the components of a possible strain vector potential.

Analytical expressions can be found for the Landau level eigenstates in a homogeneous magnetic field, arbitrary intrinsic and Rashba SOC, in the absence of potential and strain-induced vector potential [18].

In recent work, Bercioux *et al.* [13] have focused on the effects of intense SOC and a perpendicular magnetic field on the electronic properties of a graphene p-n junction (see figure 1.4). For this purpose, the system is described in terms of a low-energy Dirac-Weyl Hamiltonian [13]. The model takes into account pristine graphene, SOC terms (Rashba and intrinsic), the potential step, and the perpendicular magnetic field,

$$\begin{aligned} H = H_G + V + H_Z + H_{RSO} + H_{ISO} : \\ H_G = v_f(\tau_z s_0 \sigma_x \Pi_x + \tau_0 s_0 \sigma_y \Pi_y), \\ H_Z = \mu_B B s_z, \\ H_{ISO} = S_1 \tau_z s_z \sigma_z, \\ H_{RSO} = R(\tau_z s_y \sigma_x - \tau_0 s_x \sigma_y), \end{aligned} \tag{1.9}$$

where $\Pi = \mathbf{p} + \frac{e}{c}\mathbf{A}$, **A** and V are the vector and scalar potentials, respectively. H_Z is the Hamiltonian that represents the Zeeman field, H_{ISO} is the intrinsic SOC and H_{RSO} is the Rashba SOC.

In this work, they introduce a potential to create an interface separating region p from region n at x=0,

$$V = V_0 sgn(x), \; V_0 > 0. \tag{1.10}$$

Moreover, the vector potential is **A**= (0, Bx, 0), which implies a translational invariance along y-direction ($P_y = \hbar k_y$ is a good number). The eigenstates of this Hamiltonian have the following form:

$$\Psi(x, y) = e^{ik_y y} \phi^{K,K'}(x). \tag{1.11}$$

The eight component function $\phi^{K,K'}(x)$ is written in the same basis than Eq.1.7. On this subject, it is important to remark that the effective Hamiltonian as written, it assumes the decoupling of K and K' valleys. Indeed, this Hamiltonian can describe K and K' valleys separately, which signifies that

$$\phi^{K,K'}(x) = \begin{pmatrix} \phi^K(x) \\ \phi^{K'}(x) \end{pmatrix}. \tag{1.12}$$

Finally, Bercioux *et al.*, using the decoupled basis, found the exact solutions for graphene p-n junction under the action of a constant potential and the eigenstates for the potential step were determined. This allows them to characterize the spectrum of dispersive Landau levels. Near to the zero level they found linearly dispersing zero modes with wave-vector-dependent spin polarization [13].

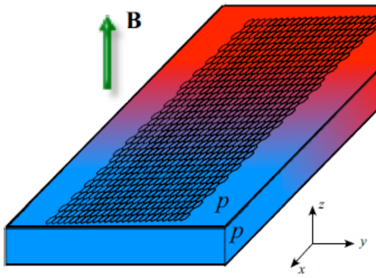

Figure 1.4: Squematic representation of graphene p-n junction [13]

To summarize, the proximity effect of TMD on graphene is modeled through a low-energy effective Hamiltonian. This Hamiltonian takes into account the preserved and broken symmetries. Therefore, the changes in the energy band structure of graphene, due to intrinsic SOC, Rashba SOC, energy differences between sublattices A and B, and an external magnetic field, are contained in the eigenstates of this Hamiltonian. In the following chapters, we will be focused on the modifications introduced on graphene electronic states for different regimes of SOC and orientations of the magnetic field.

Chapter 2

Proximity effect in hG-TMD and magnetic fields

This section is going to describe graphene and TMD heterostructure in proximity, at the same time that a magnetic field along the plane and perpendicular to the structure are applied. In this sense, it will present each one of the two cases, explaining the differences between the Hamiltonian that describes each system, as well as their energy band structures and spin textures.

2.1 General considerations of the model

According to Singh *et al.* [2], the layer of graphene is separated by a few Å (≈ 3.4 Å) from the TMD sheet.

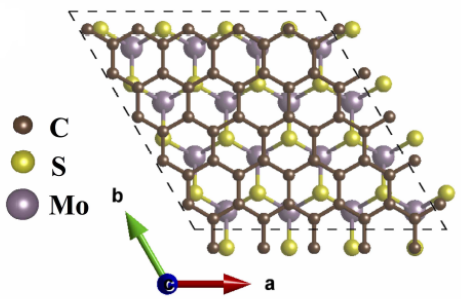

Figure 2.1: Schematic representation of graphene deposited on molybdenum disulfide (MoS_2) [2].

This heterostructure is described by effective Hamiltonian of Eq. 1.5, and its explicit form is given in Eq.1.6. Taking into account these definitions, we are able to write the matrix form of the effective Hamiltonian, as given in Eq. 2.1.

$$H_{eff} = \begin{bmatrix} \Delta + S_1 + S_2 & v_f(p_x - ip_y) & 0 & 0 & 0 & 0 & 0 & 0 \\ v_f(p_x + ip_y) & -\Delta - S_1 + S_2 & -2iR & 0 & 0 & 0 & 0 & 0 \\ 0 & 2iR & \Delta - S_1 - S_2 & v_f(p_x - ip_y) & 0 & 0 & 0 & 0 \\ 0 & 0 & v_f(p_x + ip_y) & -\Delta + S_1 - S_2 & 0 & 0 & 0 & 0 \\ 0 & 0 & 0 & 0 & \Delta - S_1 - S_2 & v_f(-p_x - ip_y) & 0 & 2iR \\ 0 & 0 & 0 & 0 & v_f(-p_x + ip_y) & -\Delta + S_1 - S_2 & 0 & 0 \\ 0 & 0 & 0 & 0 & 0 & 0 & \Delta + S_1 + S_2 & v_f(-p_x - ip_y) \\ 0 & 0 & 0 & 0 & -2iR & 0 & v_f(-p_x + ip_y) & -\Delta - S_1 + S_2 \\ . & & & & & & & \end{bmatrix} \tag{2.1}$$

The units are such that energies are given in terms of meV, velocity in m/s and momentum coordinates k_i in $1/m$. Values and orders of magnitude typical in this effective Hamiltonian are:

$$\begin{aligned} \Delta &= 0.506\ meV, \\ \hbar &= 6.582119569 * 10^{-13}\ meVs, \\ v_f &= 10^6\ \frac{m}{s}, \\ S_1 &\in [-0.16, 0.16]\ meV, \\ S_2 &\sim meV, \\ R &= 0.1\ meV. \end{aligned}$$

Because the effective Hamiltonian commutes with p_x and p_y, it is possible to write $p_x = \hbar k_x$ y $p_y = \hbar k_y$. In order to plot the band structure and spin textures, the momentum coordinates here are considered within the interval $k_x, k_y =: [-\frac{2\pi}{3a1000}, \frac{2\pi}{3a1000}]$, where $a = 1.42\,\text{Å}$ is the distance between two atoms of carbon. Therefore, the order of magnitude of $k_i \sim 10^7 \frac{1}{m}$ and energy is given by $\hbar v_f k_i \sim (10^{-13} meVs)(10^6 \frac{m}{s})(10^7 \frac{1}{m}) \sim meV$. It is worth noting that the linear momentum dependency in Eq. 2.1 is valid up to $\hbar v_f k_i \sim 1eV$.

Nonetheless, it is important to note that p_x and p_y can not be always written as constants. This will occur when an external magnetic field (**B**) is applied. Thus, the election of the gauge, which defines the expression for B according to chosen direction, it is going to be crucial since the vector potential (**A**) will tell us whether a given momentum component p_i is a constant of motion.

The matrix form of H_{eff} allows us to identify terms involved in the description of the system in both K and K' valleys, which means that the eigenstates information is obtained for both valleys. Accordingly to the above-mentioned in Chapter 1, the effective Hamiltonian assumes the decoupling of K and K' valleys. In Eq. 2.1 the first four rows and columns give the terms involved in the description of the system for the K valley; on the other hand, the last four rows and columns correspond to K' valley. This implies that the 8x8 matrix can be re-expressed as two 4x4 matrices: one block for K and the other one for K' valley. From this perspective, it is possible to obtain separately the eigenstates of the hG-TMD for K and K' valleys. In each valleys, the basis $(\psi_{A,B\uparrow,\downarrow K,K'})^T$ in the absence of normal B-fields.

H_{eff} also allows us to know the spin texture of hG-TMD, which is the expectation value of the z component of the spin for a particular set of values of k_x and k_y. Thus, the eigenvectors ψ_{E,k_x,k_y} of H_{eff} play an important role:

$$\langle S_z \rangle = \left\langle \psi_{E,k_x,k_y} \middle| S_z \middle| \psi_{E,k_x,k_y} \right\rangle , \tag{2.2}$$

$\langle S_z \rangle = S_z(k_x, k_y)$ is the function that will allow plotting the spin texture to recognize the S_z behavior in the momentum space. The 8x8 matrix spin according with the selected basis is given by:

$$S_z = \frac{\hbar}{2} \begin{bmatrix} 1 & 0 & 0 & 0 & 0 & 0 & 0 & 0 \\ 0 & 1 & 0 & 0 & 0 & 0 & 0 & 0 \\ 0 & 0 & -1 & 0 & 0 & 0 & 0 & 0 \\ 0 & 0 & 0 & -1 & 0 & 0 & 0 & 0 \\ 0 & 0 & 0 & 0 & 1 & 0 & 0 & 0 \\ 0 & 0 & 0 & 0 & 0 & 1 & 0 & 0 \\ 0 & 0 & 0 & 0 & 0 & 0 & -1 & 0 \\ 0 & 0 & 0 & 0 & 0 & 0 & 0 & -1 \end{bmatrix} . \tag{2.3}$$

Of course, this matrix also assumes the decoupling of K and K' valleys. Therefore, it can be re-written as two 4x4 matrices.

2.2 Effective Hamiltonian and Magnetic Fields

The formulation for both cases, without and with the applied magnetic field, are discussed now.

2.2.1 hG-TMD

Taking into account the above-mentioned points, this section will be focused in the energy band structure, as well as the spin texture, in two cases: when $\mid S_1 + S_2 \mid > \Delta$ and $\mid S_1 + S_2 \mid < \Delta$.

In the case of no magnetic external field, only the proximity of TMD affects the graphene band structure (see figure 2.1). Furthermore, p_x and p_y are constants of motion due to their commutation with H_{eff}. The Hamiltonian has the following form around K valley:

$$H_{eff}{}^{K} = \begin{bmatrix} \Delta + S_1 + S_2 & v_f\hbar(k_x - ik_y) & 0 & 0 \\ v_f\hbar(k_x + ik_y) & -\Delta - S_1 + S_2 & -2iR & 0 \\ 0 & 2iR & \Delta - S_1 - S_2 & v_f\hbar(k_x - ik_y) \\ 0 & 0 & v_f\hbar(k_x + ik_y) & -\Delta + S_1 - S_2 \end{bmatrix}, \tag{2.4}$$

and S_z for the K valley is:

$$S_z{}^{K} = \frac{\hbar}{2} \begin{bmatrix} 1 & 0 & 0 & 0 \\ 0 & 1 & 0 & 0 \\ 0 & 0 & -1 & 0 \\ 0 & 0 & 0 & -1 \end{bmatrix}. \tag{2.5}$$

Eigenenergies of Eq. 2.4 allow one to know the energy band structure of the system, while eigenvectors are relevant in order to visualize the behaviour of spin in k space and its relation to the band structure.

2.2.2 hG-TMD under magnetic field along the plane

Now an external magnetic field along the plane is introduced. Two directions of the field are considered, namely, $\mathbf{B}= B\hat{\mathbf{x}}$ and $\mathbf{B}= B\hat{\mathbf{y}}$. Vector potentials were selected as $\mathbf{A}= (0, 0, By)$ and $\mathbf{A}= (0, 0, -Bx)$, respectively. From this perspective, both p_x and p_y remain constant because they still commute with H_{eff}.

The Hamiltonian associated to the Zeeman interaction between the magnetic field and the spin is given by:

$$H_{int} = -\boldsymbol{\mu} \cdot \mathbf{B}, \tag{2.6}$$

with $\mu=\frac{-e}{m_e c}\mathbf{S}$ and $\mathbf{S}=\frac{\hbar}{2}s_i$. Besides, the Bohr magneton is $\mu_B=\frac{e\hbar}{2m_e c}$. Therefore,

$$H_{int}=\mu_B s_i B_i. \tag{2.7}$$

The matrix form of S_x and S_y in the K valley[1] is given by:

$$S_x{}^K=\frac{\hbar}{2}\begin{bmatrix}0&0&1&0\\0&0&0&1\\1&0&0&0\\0&1&0&0\end{bmatrix},\quad S_y{}^K=\frac{\hbar}{2}\begin{bmatrix}0&0&-i&0\\0&0&0&-i\\i&0&0&0\\0&i&0&0\end{bmatrix}, \tag{2.8}$$

Taking into account Eqs. 2.4, 2.7 and 2.8 it is possible to build the total effective Hamiltonian, that is:

$$H_T=H_{eff}+H_{int}. \tag{2.9}$$

It is also possible to analyze different regimes for the magnitude of the magnetic field, as it will be shown later on.

2.2.3 hG-TMD under perpendicular magnetic field

When a magnetic field is applied along the z-direction, the gauge plays an important role: it defines which observables are conserved. In this case, following De Martino *et al.* [18], the selected gauge is:

$$\mathbf{A}=(-By,0,0). \tag{2.10}$$

For this choice, the momentum $p_x=\hbar k_x$ is a conserved quantity, while $p_y=i\hbar\partial_y$ is not. Taking into account Eqs. 2.7 and 2.5, we can write the interaction Hamiltonian and add it to H_{eff} in order to obtain the total Hamiltonian (H_T) of the system.

$$H_T{}^K=\begin{bmatrix}\Delta+S_1+S_2+b & v_f(\Pi_x-ip_y) & 0 & 0\\ v_f(\Pi_x+ip_y) & -\Delta-S_1+S_2+b & -2iR & 0\\ 0 & 2iR & \Delta-S_1-S_2-b & v_f(\Pi_x-ip_y)\\ 0 & 0 & v_f(\Pi_x+ip_y) & -\Delta+S_1-S_2-b\end{bmatrix} \tag{2.11}$$

---

[1] These matrices are identical for K' valley.

where $b \equiv \mu_B B$, and $\Pi \equiv p_x + \frac{e}{c}(-By)$.

Due to the conservation of k_x, the eigenstates take the form:

$$\Psi_K(x, y) = e^{ik_x x}\phi_K(y). \tag{2.12}$$

In order to find the eigenstates associated to 2.12, dimensionless quantities are introduced: lengths are expressed in terms of the magnetic length $l_B = \sqrt{\frac{\hbar c}{2eB}}$, wave vectors in units of ${l_B}^{-1}$ and energies in terms of $\hbar\omega_c = \frac{\hbar v_f}{l_B}$. From this perspective, it is possible to propose a new dimensionless variable [18]:

$$\eta = y - 2k_x, \tag{2.13}$$

and some auxiliary parameters:

$$\begin{aligned} \mu_\pm &= E + b + S_2 \pm S_1 \mp \Delta, \\ \nu_\pm &= E - b - S_2 \pm S_1 \pm \Delta. \end{aligned} \tag{2.14}$$

Then, we can rewrite the total Hamiltonian as:

$$E - {H_T}^K = \begin{bmatrix} \nu_- & a & 0 & 0 \\ a^\dagger & \nu_+ & 2iR & 0 \\ 0 & -2iR & \mu_+ & a \\ 0 & 0 & a^\dagger & \mu_- \end{bmatrix}, \tag{2.15}$$

where the ladder operators are defined as:

$$a = \frac{\eta}{2} + \partial_\eta \ , \ a^\dagger = \frac{\eta}{2} - \partial_\eta \ , \ [a, a^\dagger] = 1. \tag{2.16}$$

The eigenvalues and eigenvectors are obtained by solving the equation:

$$(E - {H_T}^K)\phi(\eta) = 0 \tag{2.17}$$

where $\phi(\eta)$ is a four component spinor in K valley that takes into account the sublatices A/B and spin-up/spin-down. The solution of Eq. 2.17 is given in terms of parabolic cylinder functions (see Appendix A) $D_p(\eta), D_p(-\eta)$ as follows:

$$\phi_{K,p} = \begin{pmatrix} -pD_{p-1}(\eta) \\ \nu_- D_p(\eta) \\ i\frac{\nu-p}{2R}D_p(\eta) \\ -i\frac{\nu-p}{\mu_- 2R}D_{p+1}(\eta) \end{pmatrix}, \begin{pmatrix} pD_{p-1}(-\eta) \\ \nu_- D_p(-\eta) \\ i\frac{\nu-p}{2R}D_p(-\eta) \\ i\frac{\nu-p}{\mu_- 2R}D_{p+1}(-\eta) \end{pmatrix}. \tag{2.18}$$

Besides, from Eq. A.8 we obtain that p is related to the energy:

$$p = \frac{1}{2}[\mu + \nu - 1 \pm \sqrt{(\mu + \nu - 1)^2 + 4((2R)^2\mu_-\nu_- + \nu(1-\mu))}], \tag{2.19}$$

where

$$\begin{aligned} \mu = \mu_+\mu_- &= (E + b + S_2)^2 - (S_1 - \Delta)^2, \\ \nu = \nu_+\nu_- &= (E - b - S_2)^2 - (S_1 + \Delta)^2, \\ \mu_-\nu_- &= (E - S_1)^2 - (b + S_2 + \Delta)^2. \end{aligned} \tag{2.20}$$

From Eq. 2.19 it is found the following expression for energy in terms of p:

$$\begin{aligned} [(E + b + S_2)^2 - (p + 1 + (S_1 - \Delta)^2)] + \\ [(E - b - S_2)^2 - (p + (S_1 + \Delta)^2)] = \\ (2R)^2[(E - S_1)^2 - (b + S_2 + \Delta)^2]. \end{aligned} \tag{2.21}$$

The eigenstates associated with Eq. 2.17 are completely defined. Thus, we will analyze the behavior of the energy as a function of the magnetic field strength in the two regimes: inverted band and direct bandgap. Moreover, we will study the influence of Rashba term in the energy bands.

2.3 Changes in hG-TMD

The effective Hamiltonian includes electronic properties of hG-TMD between the spin-orbit coupling given by the parameters S1 and S2, and the presence of the TMD as included by the main bandgap Δ. Two regimes are considered here, when the SOC is strong ($\mid S_1 + S_2 \mid > \Delta$) and weak ($\mid S_1 + S_2 \mid < \Delta$).

2.3.1 Effects of proximity hG-TMD

a) Strong SOC regime

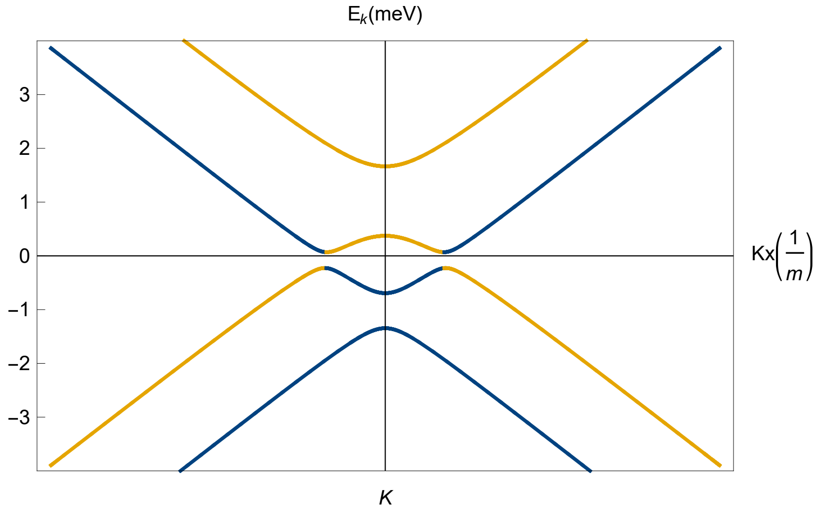

Figure 2.2: Band structure in the regime of *inverted band* when $|S_1 + S_2| > \Delta$. Color of curves indicates majority spin S_z projection. Blue ↓, yellow ↑.

The figure 2.2 shows the energy band structure of hG-TMD as a function of k_x in the K valley. The proximity effects take place, with $S_1 = 0.16meV$, $S_2 = 1.0meV$, $R = 0.1meV$ and $\Delta = 0.506meV$. The lower (upper) band is blue (yellow), which means that the spin is entirely negative (positive). On the other hand, the second (third) band is yellow (blue) for all values of k, except those close to zero, when the spin changes from positive (negative) to negative (positive).

Using Eqs. 2.2 and 2.5 the corresponding spin texture for this regime is obtained. Spin texture allows us to understand how the spin is modified depending on momentum. Upper row in figure 2.3a shows a section along the k_x axis of the spin texture for band structure around K valley in units of $\hbar$. The number at the right side of each curve means the number of the band from the bottom to the top in figure 2.2. Thus, the curve with number 1 represents the value of spin projection along z for the lower band in 2.2; the number 2 associates the S_z value with the second band in the corresponding band structure and so on. The lower row (see figure 2.3b) represents spin texture for the section of the Brillouin zone $k_x, k_y =: [-\frac{2\pi}{3a1000}, \frac{2\pi}{3a1000}]$. In what follows this window for momenta will be used.

On the lower row, the first square (from left to right) represents the spin of the lower band in the band structure in figure 2.2: spin entirely takes negative values. This changes when we analyze the second and the third bands. Second square shows that spin is positive for all values of k_x, k_y except for those close to zero, where spin becomes negative. The third square displays the fact that spin is negative for all values of momentum except for those close to Dirac point, where spin is positive. The last square represents the spin of the upper band; spin is positive for all k values.

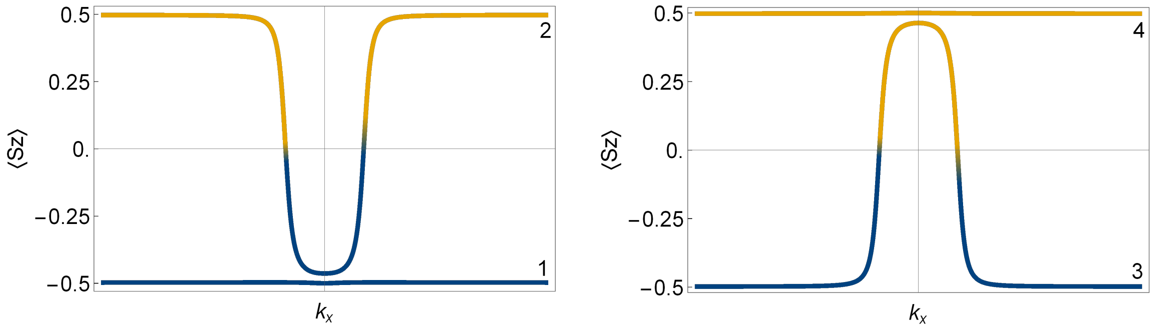

(a) $S_z(k_x)$

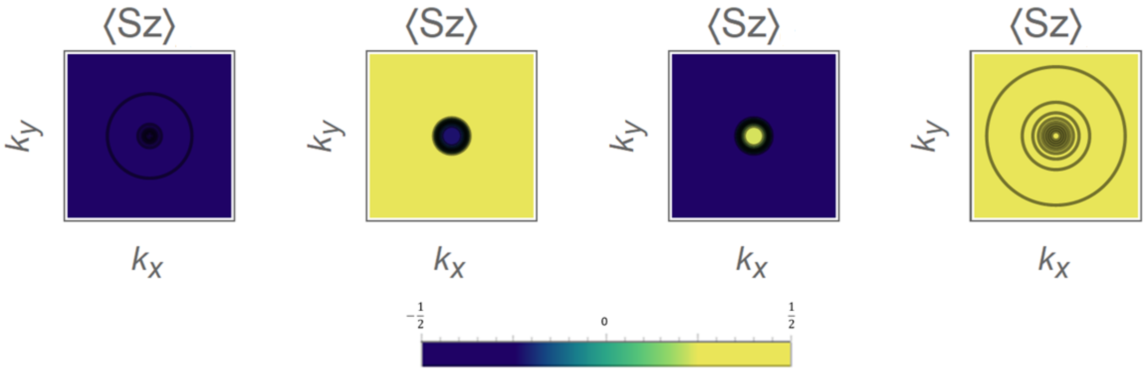

(b) $S_z(k_x, k_y)$

Figure 2.3: $\mid S_1 + S_2 \mid > \Delta$ regime. From left to right the spin projection along the z-axis is shown from the lowest energy band to the highest one. a) Spin texture along k_x axis ($k_y = 0$). b) Spin texture for all k_i values; yellow means that spin has positive values, otherwise blue represents the negative ones.

To sum up, the color of spin texture changes for values of k_x or k_y close to K point in the second and third bands. This means that an inversion of spin has taken place in those values due to high spin-orbit coupling and the Rashba term, allows for the mixing when nearly degenerate branches cross.

b) Weak SOC regime

On the other hand, the energy band structure of hG-TMD changes when the SOC parameter are small such that $S_1 = 0.0005meV$ and $S_2 = 0.32meV$ (with $R = 0.1mev$ and $\Delta = 0.506meV$) as is presented in figure 2.4, where the lower energy band, as well as the third, is blue because the spin is negative. The second and fourth bands are yellow due to the positive values of the spin. Thus, in this case there is not a spin band inversion.

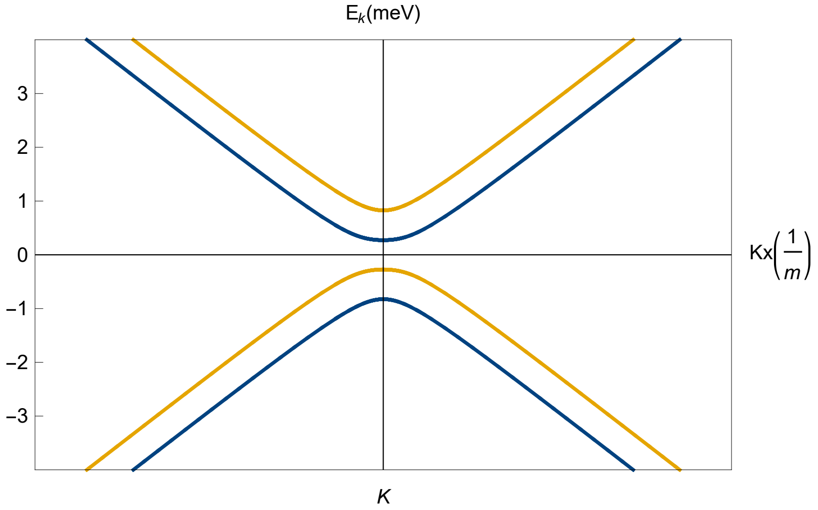

Figure 2.4: Band structure in the regime of *direct bandgap* when $|S_1 + S_2| < \Delta$,i.e., weak SOC.

As before, the upper row in figure 2.5a is a cross-section of spin texture, and the lower row in figure 2.5b shows the entire spin texture.

The first and third squares (from left to right) depict the spin of the lower and third bands, respectively, according to figure 2.4: spin is negative in both cases. Similarly, the second and fourth squares show that spin is positive for all k values. Therefore, in the regime of direct bandgap spin projection along z axis does not change direction, which implies that the SOC terms were not strong enough to compete with staggered potential Δ that yield to the inversion of bands.

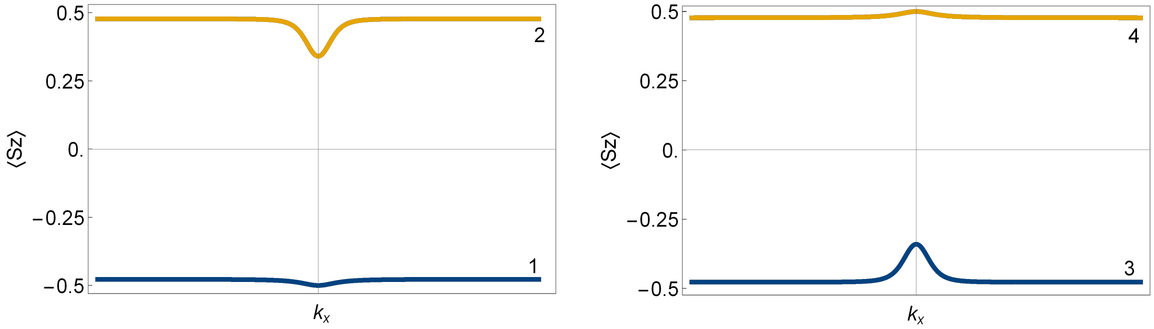

(a) $S_z(k_x)$

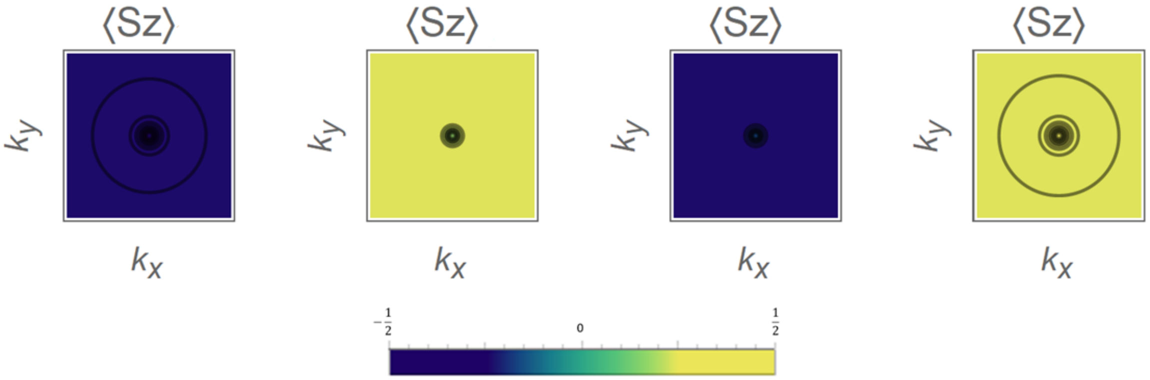

(b) $S_z(k_x, k_y)$

Figure 2.5: $\mid S_1 + S_2 \mid < \Delta$ regime. From left to right, the spin projection along the z-axis is shown from the lowest energy band to the highest one. a) Spin texture when $k_y = 0$. This perspective allows us to know the values of the S_z. b) Spin texture for all k_i values; yellow means that spin has positive values, otherwise blue represents the negative ones. According to these textures, spin remains entirely positive or negative: there is no inversion band.

To finalize, it is remarkable that all spin textures (figures 2.3b and 2.5b) display circular contours, which means that energy band structures and spin textures are radially symmetric around the K point, otherwise these circular contours would disappear.

2.3.2 Effect of a magnetic field applied on the plane

a) Strong SOC and B along x direction

This section will consider two cases: the first one, when the magnetic field is $B = 4T$ and the second one, for $B = 40T$, in order to compare the effects of weak and strong magnetic fields, respectively. This will give insight on how to control the spin by means of external fields, an issue of interest for applications in spintronics. The values of S_1 and S_2 were expressed in the previous section.

Low magnetic field.

When the magnetic field is weak ($B = 4T$), the magnetic energy is $\approx 0.23meV$. The energy band structures do not change much from those we have seen in the last section (see figure 2.2). Nonetheless, it is important to point out that the symmetry along k_x is not the same as the one for k_y, as seen in figure 2.6.

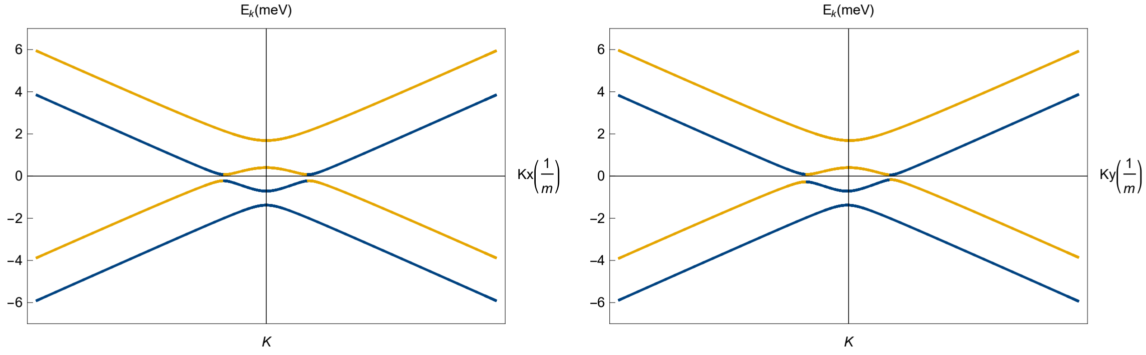

(a) $E(k_x)$ (b) $E(k_y)$

Figure 2.6: Band structure in the regime of *inverted band* when $|S_1 + S_2| > \Delta$ and magnetic energy $\approx 0.23meV$. a) Band structure for $k_y = 0$. b) Band structure for $k_x = 0$.

As the magnetic field along x direction affects the band structure, the same happens to the spin textures, which is more visible when we separately analyze the cross sections along both k_x and k_y axes.

In figure 2.7, the upper (lower) row shows the spin projection along z direction as a function of k_x (k_y). The symmetry of these textures remains (does not remain) along k_x (k_y). This is possible to see when we compare, for example, the second S_z curve in figure

2.7a with the second one of figure 2.7b: the minimal value in the first case is around $k_x = 0$ while in the second case, this value is found for a $k_y \neq 0$.

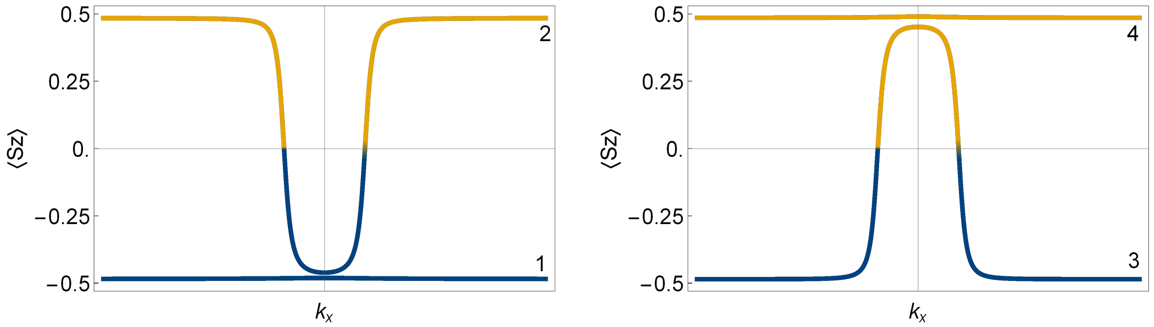

(a) $S_z(k_x)$

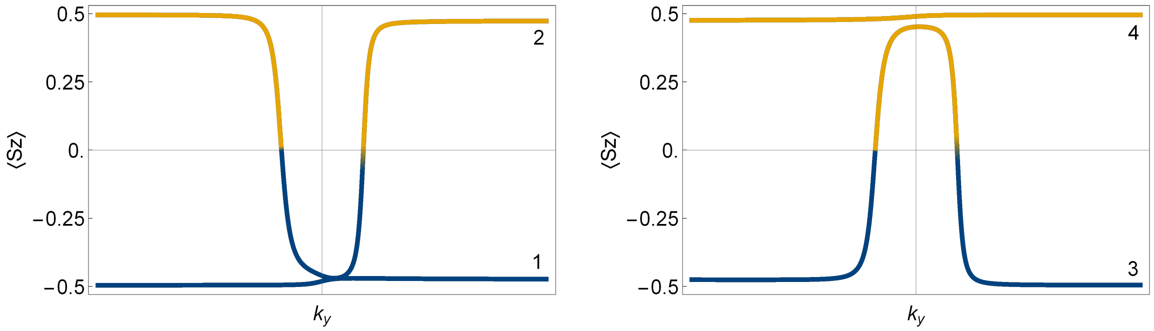

(b) $S_z(k_y)$

Figure 2.7: Cross sections of spin projection along z axis in the regime of spin inverted band with a magnetic energy of $\approx 0.23meV$. a) Spin texture for $k_y = 0$. b) Spin texture for $k_x = 0$.

The first (fourth) square is entirely dark blue (yellow), which means that the lower (upper) band has negative (positive) spin. The second and third bands presented an inversion of spin for values of k_x and k_y around Dirac point, which can be seen in the second and third squares of spin texture.

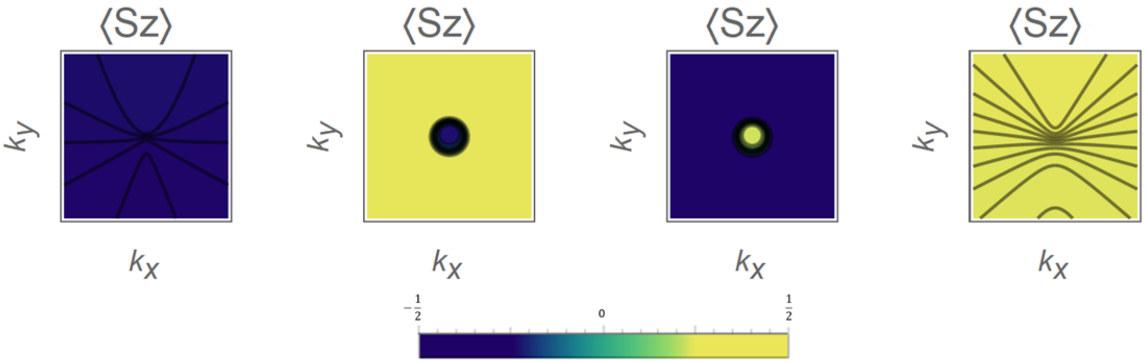

Figure 2.8: Spin texture when $\mathbf{B}$=$4T$ and $|S_1 + S_2| > \Delta$. Taking into account the second and third squares, it is possible to see that spin band inversion around K point persists for small magnetic fields.

Strong magnetic field.

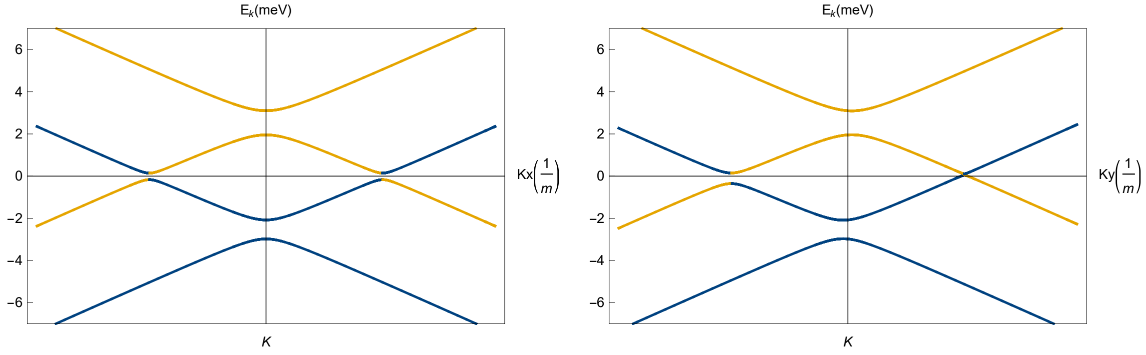

(a) $E(k_x)$ (b) $E(k_y)$

Figure 2.9: Band structure in the regime of *inverted band* when $|S_1+S_2| > \Delta$ and magnetic energy $\approx 2.3meV$. a) Band structure for $k_y = 0$. b) Band structure for $k_x = 0$.

As for an intense magnetic field in the $\mid S_1 + S_2 \mid > \Delta$ regime, the energy increases, as well as its bandwidth, in the inverted band zone. Besides, the lack of symmetry of the band structure and cross section of spin texture along k_y are more notorious.

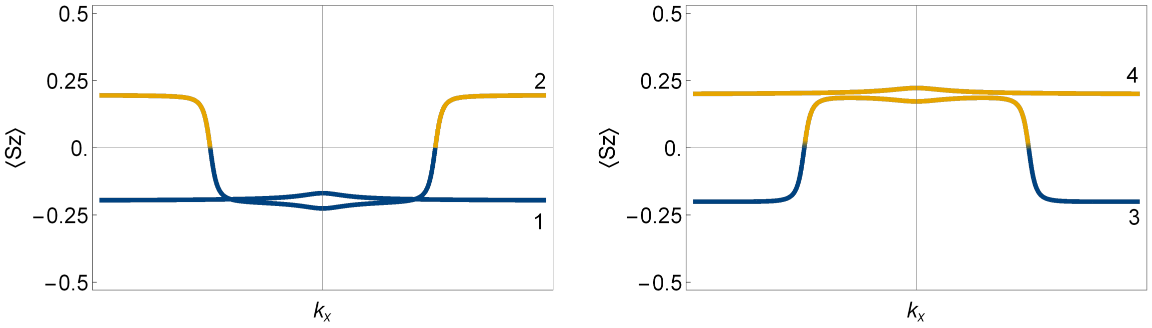

(a) $S_z(k_x)$

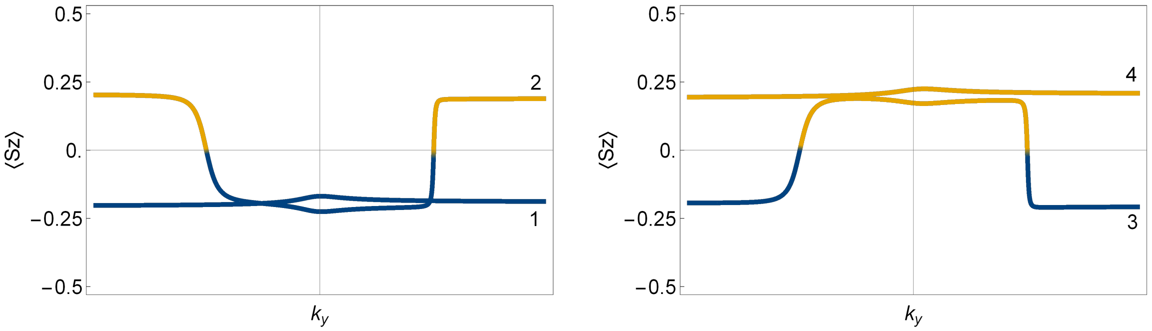

(b) $S_z(k_y)$

Figure 2.10: Cross sections of spin projection along z axis in the regime of spin inverted band with a magnetic energy of $\approx 2.3meV$. a) Spin texture for $k_y = 0$. b) Spin texture for $k_x = 0$.

Additionally, in figure 2.10 it can be seen that spin does not reach the possible minimal $(-1/2)$ or maximal $(1/2)$ values. Hence, the color of the spin texture in figure 2.11 oscillates from light blue to light green. This behavior can be understood as follows: when the magnetic field becomes intense, the spin couples to field aligning to its direction. In this sense, the spin projection along x-direction will reach the minimal or maximal values, as the external field competes with the strong SOC intrinsic to the system.

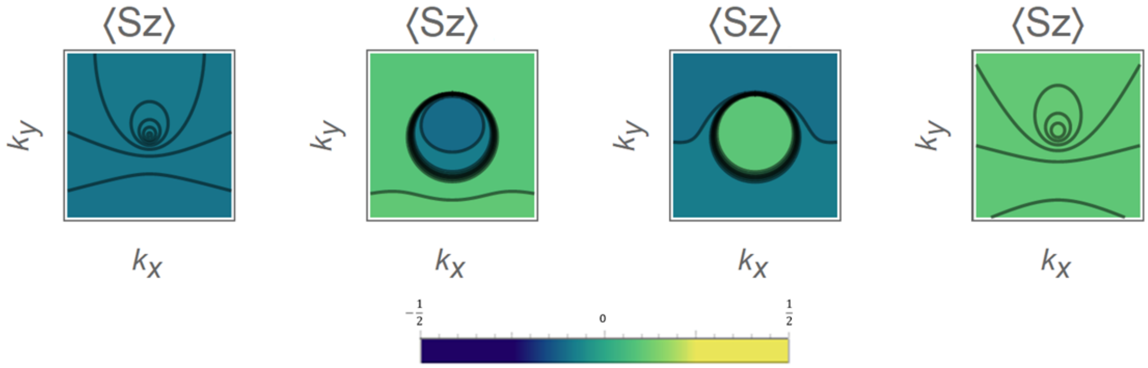

Figure 2.11: Spin texture when B= $40T$ and $|S_1 + S_2| > \Delta$. According to the second and third squares, the spin inversion is still present but less intense than $B = 4T$.

b) Weak SOC and B along x direction

Low magnetic field.

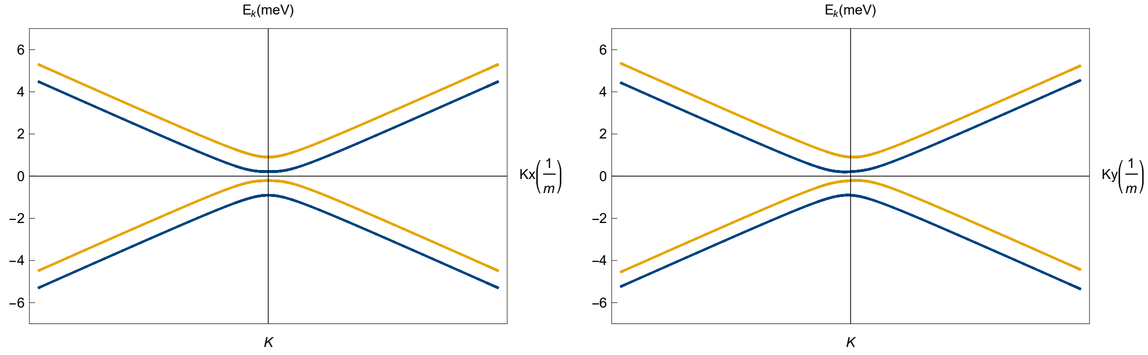

(a) $E(k_x)$ (b) $E(k_y)$

Figure 2.12: Band structure in the regime of *direct band gap* when $|S_1 + S_2| < \Delta$ and magnetic energy $\approx 0.23meV$. a) Band structure for $k_y = 0$. b) Band structure for $k_x = 0$.

When SOC is smaller than Δ spin inversion is not seen. In this particular case, a small magnetic field is applied along x direction (magnetic interaction is 0.23meV). The symmetry of band structure, as well of the spin texture, are broken along the k_y direction (see specially figures 2.12b and 2.13b).

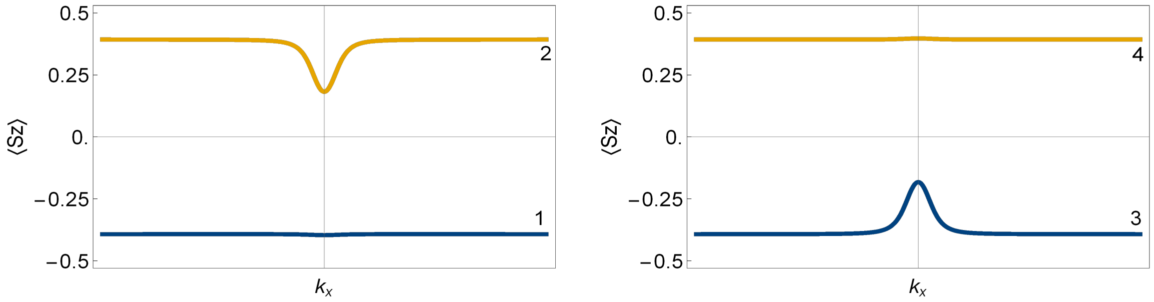

(a) $S_z(k_x)$

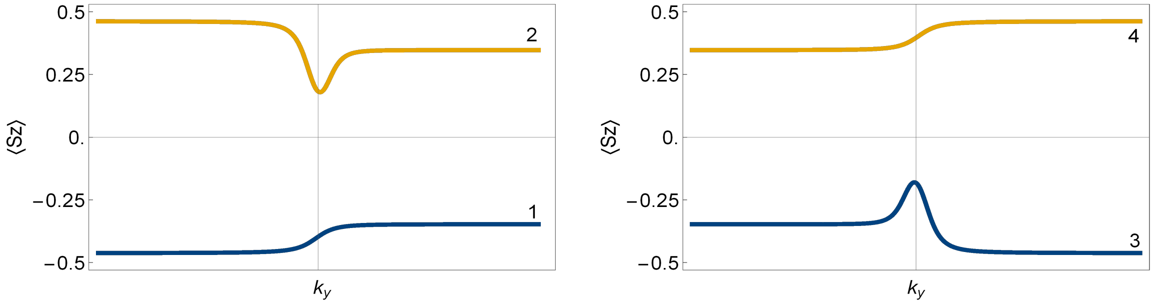

(b) $S_z(k_y)$

Figure 2.13: Cross sections of spin projection along z axis in the regime of direct band gap with a magnetic energy of $\approx 0.23meV$. a) Spin texture for $k_y = 0$. b) Spin texture for $k_x = 0$.

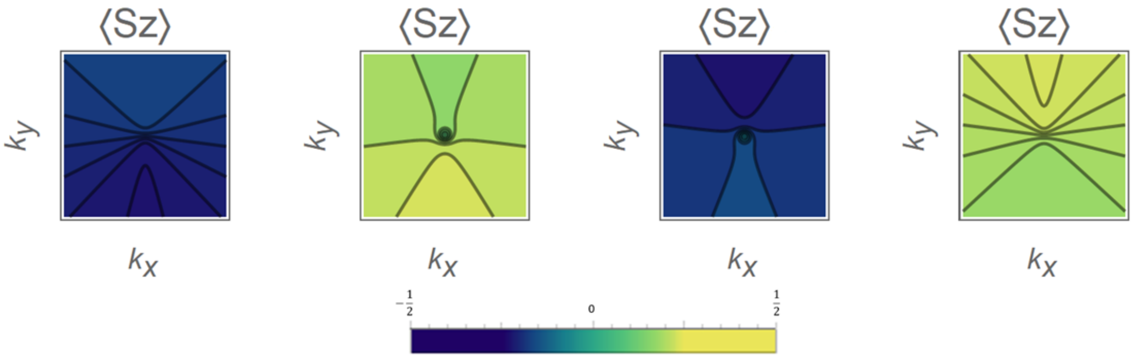

Figure 2.14: Spin texture for $B = 4T$ and $|S_1 + S_2| < \Delta$. According to the color tones of squares the spin is oscillating around its maximal and minimal values because of the presence of B.

As a result of the above mentioned, spin texture does not change in a band, from blue to yellow, because there is no spin band inversion. Although, in figure 2.14 we can see that the first (second) and third (fourth) square -from left to right- has various color tones of blue (yellow) because of a little oscillation in the spin values; these changes of color tones are more notorious in the second and the third squares, which represent the spin in the second and third band, respectively.

According to the color tones of squares the spin is oscillating around its maximal (1/2) and minimal ($-1/2$) values because of the presence of the magnetic field. Nonetheless, the strength of B is not enough to provoke an alignment of spin.

Strong magnetic field.

When the magnetic field increases, it is possible to see how a slight spin band inversion is produced between the second and third band (figure 2.15). Moreover, the symmetry of the band structure, as well as the spin, is still broken along k_y direction.

The fact that we found an inverted band when $|S_1 + S_2| < \Delta$ can be revealed in a better way when we see the cross-section of spin texture in figure 2.16a. The first square represents the values of spin in the first band of the band structure: spin is negative (its values are nearly zero). The second square represents the change of spin from positive (close to zero) to negative (also very nearly to zero) in the second band. The third one changes similarly but from negative to positive. For the last one it is entirely positive.

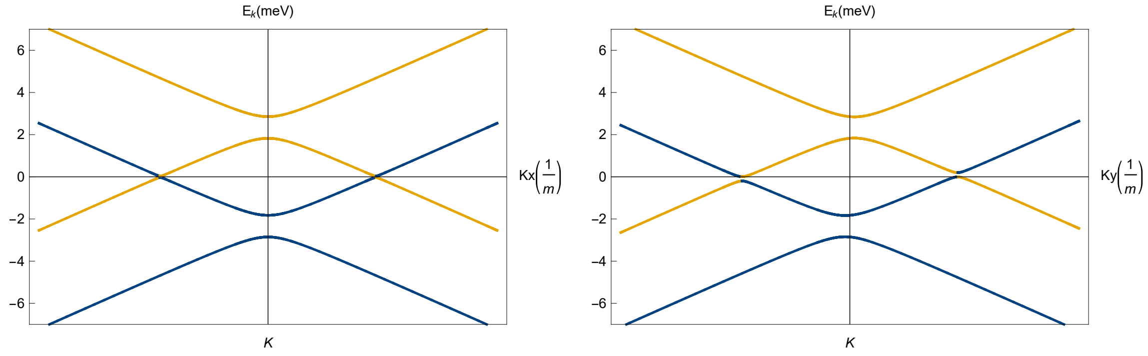

(a) $E(k_x)$ (b) $E(k_y)$

Figure 2.15: Band structure when $|S_1 + S_2| < \Delta$ and magnetic energy $\approx 2.3meV$. A small inverted band takes place in this regime due to the high magnetic field. a) Band structure for $k_y = 0$. b) Band structure for $k_x = 0$.

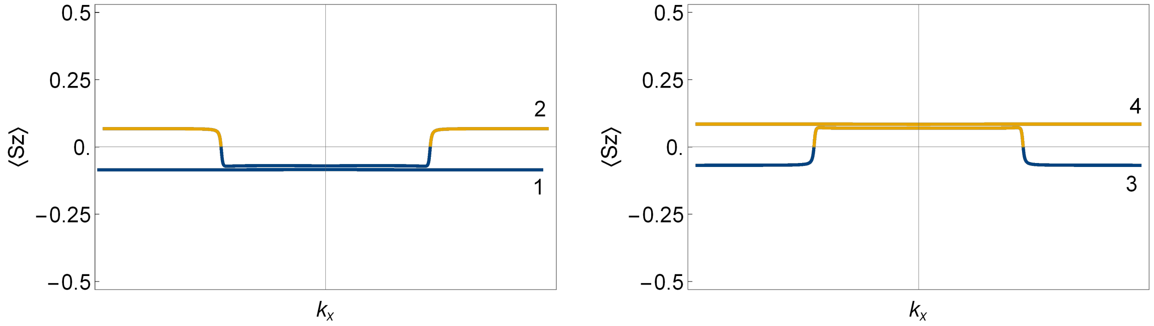

(a) $S_z(k_x)$

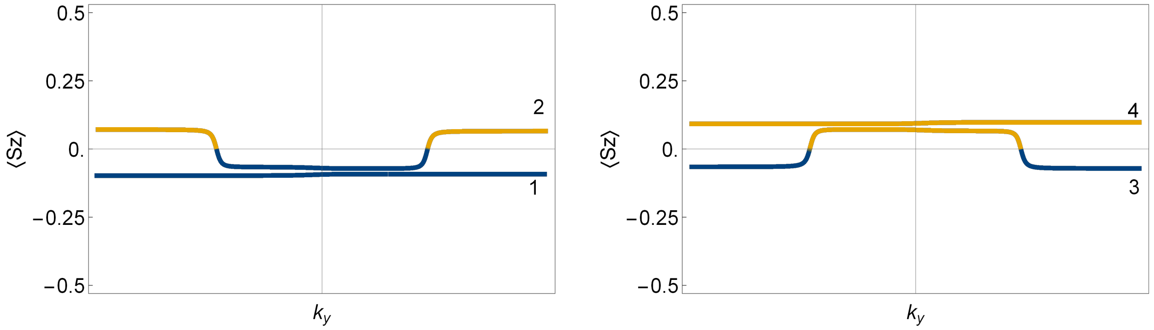

(b) $S_z(k_y)$

Figure 2.16: Cross sections of S_z in the regime weak SOC with a magnetic energy of $\approx 2.3meV$. a) Spin texture when $k_y = 0$. b) Spin texture when $k_x = 0$.

Once again, it is possible to see in figure 2.17 that spin does not reach the possible minimal or maximal values. As it was already mentioned, this happens because of the coupling causing alignment of the direction of spin and the magnetic field.

Finally, SOC and magnetic field-spin interaction energy clearly compete such that the increase of one of them can change the band structure and the behavior of spin in the graphene-TMD structure. In this case, the magnetic field is stronger and caused a slight inversion band, which implies that manipulation of spin is possible by means of an external magnetic field.

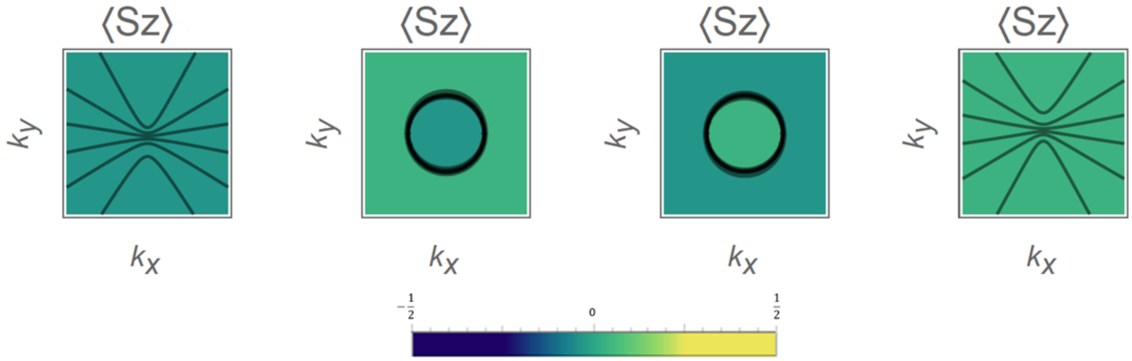

Figure 2.17: Spin texture for $\mathbf{B}$=$40T$ and $|S_1 + S_2| < \Delta$. From left to right, the first and fourth square shows defined negative and positive spin values, respectively. According to the second and third squares, a small spin inversion band has been created because of the magnetic field strength.

In order to conclude, it is found that the magnetic field on the plane changes the band structure, as well as the spin texture. Likewise, band structure symmetry is broken along the direction of the applied field[2]. Moreover, because of competition between the spin-orbit coupling and the external field a small inversion band is created, even in the *direct band* regime, whose features do not contemplate a spin inverted band in absence of a magnetic field (see figure 2.4).

2.3.3 Proximity effect hG-TMD in a perpendicular magnetic field

In the first place, we consider the case where TMD proximity effect on graphene and the Zeeman field are turned-off, that is, $\Delta = S_1 = S_2 = R = b = 0$. Eq. 2.21 reduces to the form:

$$[E^2 - (p+1)][E^2 - p] = 0. \tag{2.22}$$

It is found that this corresponds to the spin-degenerate Landau levels $E_m = \pm\sqrt{m}$ ($m = 0, 1, 2...$), where $m = p$ (spin-up) and $m = p + 1$ (spin-down). The ground state occurs for $E_m = 0$ ($p = -1, 0$) [18].

Following this, Eq. 2.21 can be manipulated by turning-on all the terms, or part of them, to analyze the competition between the interactions such as the proximity of TMD

---

[2] This also can be seen when the magnetic field is applied along y direction. Further details about this topic are in the Appendix B.

and graphene, as well as the coupling of the perpendicular magnetic field with the spin. It should be highlighted that all these parameters are dimensionless, which means that they are in units of $\hbar\omega_c$ for energy (see Eq. 2.13).

When one turns on all terms except Rashba ($R = 0$), the Landau levels are obtained but no longer-degenerate, shifted by the parameters.

$$\begin{aligned} E_m &= \pm\sqrt{p + (S_1 + \Delta)^2} + b + S_2, \\ E_m &= \pm\sqrt{p + 1 + (S_1 - \Delta)^2} - b - S_2. \end{aligned} \tag{2.23}$$

The first line corresponds to spin-up and the second one, to spin-down. Figure 2.18 shows these energies as a function of magnetic field, as included in parameter b, for $p = 0, 1$. This figure allows us to see that without Rashba term, the projection of spin along the z direction is not inverted and Landau levels also appear.

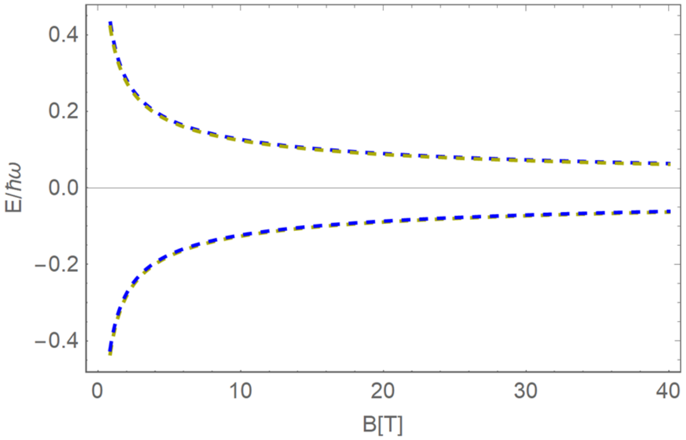

Figure 2.18: Spin Landau levels when $R = 0$ in the *direct bandgap* regime. Here, $S_1 = 0.005meV$, $S_2 = 0.32meV$ and $\Delta = 0.506meV$. Dark yellow dashed line represents spin-up and blue dashed line, spin-down. Values of energy have been multiplied by 10 in order to magnify their separation.

Taking into account Eq.2.21, now we study the energy in the *inverted band* (Strong SOC) and *direct bandgap* (Weak SOC) regimes when Rashba has a finite value.

a) Strong SOC

Figure 2.19 represents the energy as a function of B for $p = 0, 1$ (blue dashed line) and $p = 1, 2$ (red dashed line). This implies that there is a degeneracy of the energy levels, because the positive roots of Eq. 2.21, as well as the negatives ones, are equal and described in terms of two different discretized number p at the same time, which is more notorious in figure 2.19a, for $R = 0.1meV$.

On the other hand, the solutions of Eq. 2.21 start to be different when Rashba increases up to $R = 3.5meV$ and the magnetic field gets weak (see figure 2.19b). Besides, each root is described by two different discretized number p at the same time.

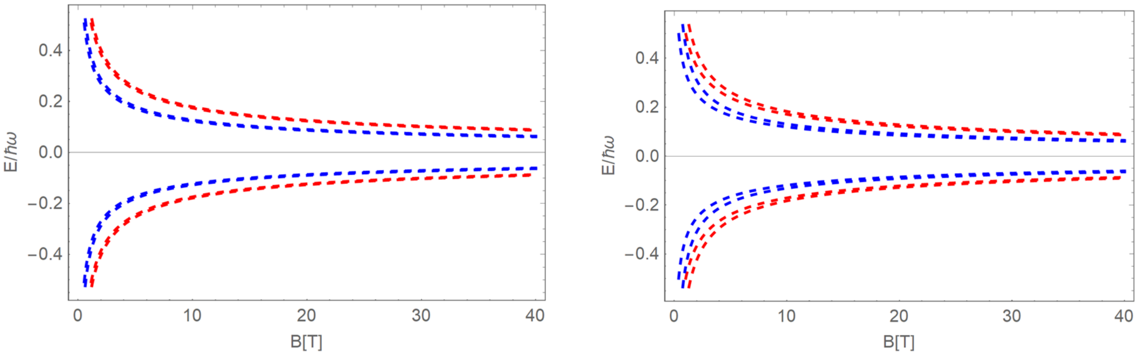

(a)

(b)

Figure 2.19: Blue dashed line is for $p = 0, 1$ and red dashed one, for $p = 1, 2$. a) Energy (in units of $\hbar\omega_c$) vs magnetic field (in tesla) for $R = 0.1meV/\hbar\omega_c$. b) Energy as a function of magnetic field for $R = 3.5meV/\hbar\omega_c$. In both cases, $S_1 = 0.16meV/\hbar\omega_c$, $S_2 = 1.0meV/\hbar\omega_c$ and $\Delta = 0.506meV/\hbar\omega_c$. Values of energy have been multiplied by 10 in order to magnify their separation.

b) Weak SOC

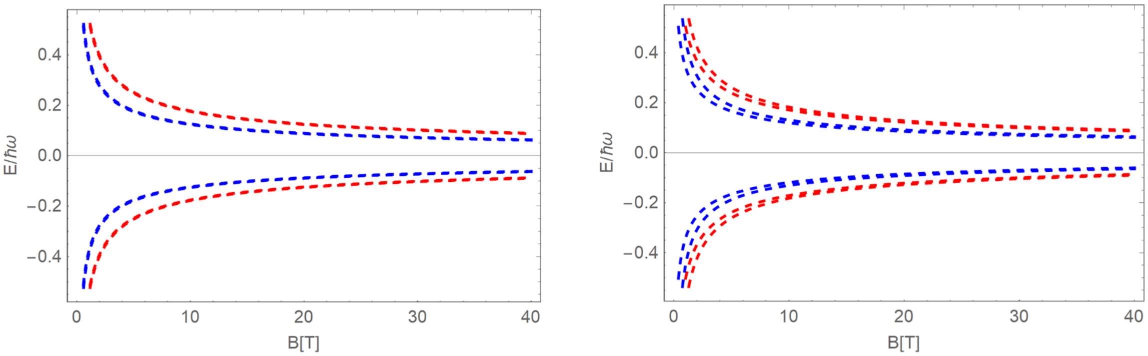

(a) (b)

Figure 2.20: The blue dashed lines shows the case for $p = 0, 1$ and the red dashed lines, for $p = 1, 2$. a) Energy vs magnetic field for $R = 0.1meV/\hbar\omega_c$. b) Energy as a function of magnetic field for $R = 3.5meV/\hbar\omega_c$. In both cases, $S_1 = 0.0005meV/\hbar\omega_c$, $S_2 = 0.32meV/\hbar\omega_c$ and $\Delta = 0.506meV/\hbar\omega_c$. Values of energy have been multiplied by 10 in order to magnify their separation.

In the *direct bandgap* regime the degeneracy of energy levels also exists as seen in figure 2.20. In this case, the degeneracy is more prominent in figure 2.20a, because all the roots of Eq. 2.21 are overlapping at the same time that are described in terms of two p numbers. Figure 2.20b is very similar to figure 2.19b.

It should also be emphasized that in these cases spin state is not pure in each level because all the solutions of the Eq. 2.21 are in terms of m not being an integer, either both p and $p + 1$, which is different from the case when $R = 0$. Therefore, it is clear that the Rashba term is responsible for spin mixing.

To conclude, it has been found that G-TMD proximity may lead to two regimes: the first one, *inverted band*, when $\mid S_1 + S_2 \mid > \Delta$; and the *direct bandgap*, with $\mid S_1 + S_2 \mid < \Delta$. In both cases the energy band structure and the spin texture is symmetric in k_x and k_y. When a magnetic field is applied along the plane, the symmetry of the energy band structure and the spin texture are preserved along the direction of the magnetic field applied, otherwise, this symmetry is broken. Moreover, it has been possible to create a mini-inverted-spin band in the regime of *direct bandgap*, which means that the manipulation of spin is allowed in the system. Finally, when the magnetic field is perpendicular to hG-TMD, the eigenstates are found analytically. Thus, it encountered that eigenvectors of the system are described in terms of parabolic cylinder functions, and eigenenergies depend on a discrete value p. When Rashba terms is zero, pure spin states and spin-degenerate Landau levels are obtained, otherwise Rashba interaction gives rise to spin mixing.

Chapter 3

Electron transport in hG-TMD

The present chapter is focused on the calculation of transmission and reflection coefficients for an incident electron that goes through graphene with a TMD ribbon of width L on top of it. This calculation has been done for two cases: the first one, for this hG-TMD in the absence of magnetic fields ; and the second one, when a magnetic field is applied along either x or y directions along the plane in the hG-TMD ribbon.

3.1 Transfer matrices in hG-TMD and magnetic field along the plane

In order to understand how the electron transport is affected by the proximity between graphene and TMD, and the effects of an external magnetic field, we have studied a system in which a ribbon of TMD, with width L of a few nm is deposited on top of a sheet of graphene, similar to those studied in experiments [9], [15]. In this sense, the system in figure 3.1 has three regions: the first and third ones are pristine graphene, and the middle region is graphene in proximity with TMD, in this zone we will apply the external magnetic fields along x or y directions.

As seen in figure 3.1, the electron propagates along the y axis, which implies that the momentum along this direction is preserved in each region but changes at the borders of the TMD. The system has three regions. In the first and third regions, the momentum of electron k_y is the same, because both zones are pristine graphene with the same Fermi energy. However, in the second region, the y-momentum changes to q_y. On the other hand, due to the traslational symmetry along the perpendicular direction, k_x is preserved in all regions. All these considerations also take into account the conservation of energy during the movement of the electron in the system. The x-momentum conservation is valid in the middle region for all cases we consider here: in the hG-TMD, with and without an external magnetic field applied along the plane.

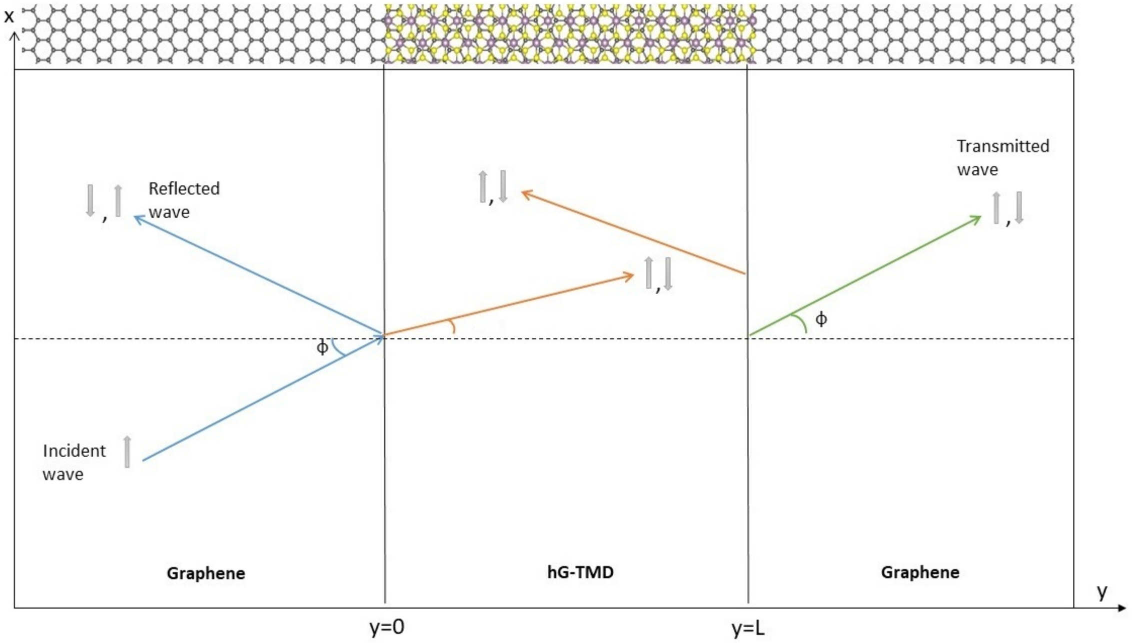

Figure 3.1: Schematic representation of the system in which an electron moves. The first and third regions are pristine graphene, the second region is hG-TMD and can be under the effects of an in-plane magnetic field. Color lines indicate the momentum while gray shor arrows the spin orientation.

The electron goes through the system with positive energies and spin-up (s=1) is chosen, while the incidence angle ($\phi = \arctan k_x/k_y$) will be modified. This allows us to recognize the role of hG-TMD (with or without a magnetic field along the plane) in the transmission and reflection probabilities of an incident electron with the spin-up or spin-down.

It is worth noting that the electron movement always occurs in graphene, but when the TMD is in proximity to graphene, the electron *feels* its presence due to the proximity effects that take place, result in the effective Hamiltonian of *Chapter 1 and 2*.

For a better understanding, let us see the scheme of the energy band structure when the electron transits from pristine graphene to hG-TM, as shown in figure 3.2. Depending on the electron's incident energy (black line) in graphene, the electron wave function can be expanded in terms of of the form $e^{ik_y y}$ when it gets in graphene and inside hG-TMD. *Quantum tunneling* occurs as the electron moves between the gaps in the energy band structure of hG-TMD, which is represented by a real q_y momentum for traveling waves under the TMD (or imaginary q_y for evanescent waves)

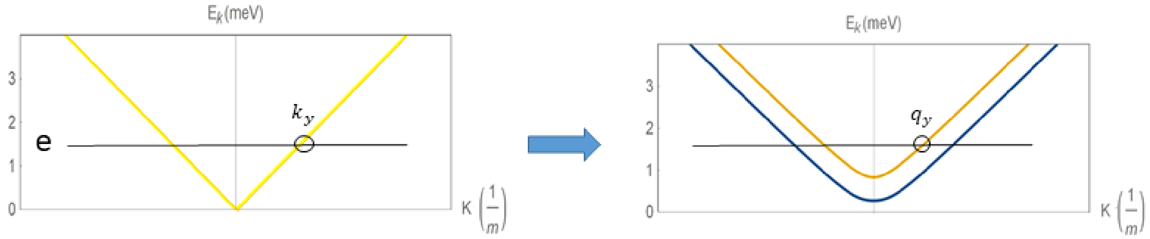

Figure 3.2: Schematic representation of the electron's motion in the energy band structure of the system in figure 3.1. Left side image is the band structure of pristine graphene near the Dirac point. Right side figure corresponds to the band structure of hG-TMD in the weak SOC regime. When electron crosses the interface $y = 0$, the band structure changes, as well as its momentum along y axis but the energy and k_x are conserved.

Wave functions of electron in the different regions are then described in terms of plane waves of the form $e^{ik_x x+ik_y y}$, which means that $p_x = \hbar k_x$ and $p_y = \hbar k_y$ are constants of motion because they commute with the effective Hamiltonian of Eqs. 2.4 and 2.9. From this perspective, the wave functions of the electron in each region are written as:

In region I:

$$\psi_I = \frac{e^{ik_x x+ik_y y}}{\sqrt{2}}\begin{pmatrix}1\\ se^{i\phi}\\ 0\\ 0\end{pmatrix} + \frac{r_1 e^{ik_x x-ik_y y}}{\sqrt{2}}\begin{pmatrix}1\\ se^{i(\pi-\phi)}\\ 0\\ 0\end{pmatrix} + \frac{r_2 e^{ik_x x-ik_y y}}{\sqrt{2}}\begin{pmatrix}0\\ 0\\ 1\\ se^{i(\pi-\phi)}\end{pmatrix}, \tag{3.1}$$

in region II:

$$\psi_{II} = a_1 e^{ik_x x+iq_{1y}y}\begin{pmatrix}A_1\\ B_1\\ C_1\\ D_1\end{pmatrix} + a_2 e^{ik_x x+iq_{2y}y}\begin{pmatrix}A_2\\ B_2\\ C_2\\ D_2\end{pmatrix} + b_1 e^{ik_x x+iq_{3y}y}\begin{pmatrix}A_3\\ B_3\\ C_3\\ D_3\end{pmatrix} + b_2 e^{ik_x x+iq_{4y}y}\begin{pmatrix}A_4\\ B_4\\ C_4\\ D_4\end{pmatrix}, \tag{3.2}$$

and in region III:

$$\psi_{III} = \frac{t_1 e^{ik_x x + ik_y y}}{\sqrt{2}} \begin{pmatrix} 1 \\ se^{i\phi} \\ 0 \\ 0 \end{pmatrix} + \frac{t_2 e^{ik_x x + ik_y y}}{\sqrt{2}} \begin{pmatrix} 0 \\ 0 \\ 1 \\ se^{i\phi} \end{pmatrix}. \tag{3.3}$$

In Eq. 3.1, the first two column vectors represent the spinors with spin-up and the third one, with spin-down. It is assumed that the coefficient that describes the amplitude of the wave function of incident up-spin electron is 1. The coefficients r_1 and r_2 are associated with the possibility that the electron would be reflected with spin-up or spin-down, respectively.

On the other hand, Eq. 3.2 describes the wave function in the middle region. In this case, the eigenvectors have a mixed spin because of the Rashba term as discussed in *Chapter 2*. All the elements A_i, B_i, C_i, D_i, with $i = 1, 2, 3, 4$, depend on k_x and q_{yi}, as well as on the structutre parameters Δ, S_1, S_2, R ; also, these terms vary according to the SOC regime and the magnetic field, if any. a_1 (b_1) and a_2 (b_2) are the coefficients that describe the electron's transmission (reflection) between $y = 0$ and $y = L$. For the Hamiltonian given by Eq. 2.4, $q_{3y} = -q_{1y}$ and $q_{4y} = -q_{2y}$ because the energy band structure for all regimes (weak and strong SOC) is symmetric. This is also valid when the magnetic field is applied along *y*. For this direction the symmetry of the energy band structure remains. Nonetheless, when the magnetic field is along x direction, the symmetry of band structured around $q_y = 0$ is broken, which implies that q_{3y} (q_{4y}) can be a little different from $-q_{1y}$ ($-q_{2y}$).

In the third region there is just graphene, then, the first spinor has spin-up, and the second one, spin-down. The coefficients t_1 and t_2 describe the electron's transmission across the system with spin-up and spin-down, respectively.

It is possible to find k_x and k_y as soon as we define the value of the electron's incident energy and the incident angle. In this case, we know the energy dispersion relation for an electron in graphene around K point is given by

$$\begin{aligned} E_G &= \hbar v_f \sqrt{k_x^2 + k_y^2}, \\ k_x &= \frac{E_G}{\hbar v_f} sin\phi, \\ k_y &= \frac{E_G}{\hbar v_f} cos\phi. \end{aligned} \tag{3.4}$$

Matching the electron's incident energy (Eq. 3.4) with the energy dispersion relation for an electron in the hG-TMD, the momenta q_{1y}, q_{2y}, q_{3y} and q_{4y} are found as roots of that equality. Given the features of the assumed incident electron -positive energy with spin-up- the energy dispersion relation in the middle region is given by the eigenvalue of the effective Hamiltonian (Eqs. 2.4 and 2.9) which corresponds to the upper band in any energy band structure shown *Chapter 2*.

$$E_G(k_x, k_y) = E_{hG-TMD}(k_x, q_y). \tag{3.5}$$

Thus, q_y is a function of k_x and k_y, which are known quantities.

Moreover, coefficients r_i, a_i, b_i and t_i are determined from the continuity of the spinor wave function: $\psi_I(x, y = 0) = \psi_{II}(x, y = 0)$ and $\psi_{II}(x, y = L) = \psi_{III}(x, y = L)$. In contrast to the Schrodinger equation, the matching of wave function derivatives is not necessary here. Taking this into account, it is possible to find the transmission and reflection probabilities as follows:

$$\begin{aligned} T_{\uparrow,\uparrow} &= t_1 {t_1}^*; \\ T_{\uparrow,\downarrow} &= t_2 {t_2}^*; \\ R_{\uparrow,\uparrow} &= r_1 {r_1}^*; \\ R_{\uparrow,\downarrow} &= r_2 {r_2}^*, \end{aligned} \tag{3.6}$$

where the coefficients represent the probabilities that an incident electron with spin up going through the graphene-TMD ribbon: $T_{\uparrow,\uparrow}$ be transmitted with spin-up; $T_{\uparrow,\downarrow}$ be transmitted with spin-down; $R_{\uparrow,\uparrow}$ be reflected with spin-up; and $R_{\uparrow,\downarrow}$ be reflected with spin-down.

In order to calculate these probabilities, we use the transfer matrix method. This allows us to analyze the wave propagation of electrons. The transfer matrix D_{y_0} relates the amplitudes of the waves to the left side of each border ($y_0 = 0$ or $y_0 = L$) in terms of those on the right side [19].

Therefore, from the first boundary condition $\psi_I(x, y = 0) = \psi_{II}(x, y = 0)$, the amplitudes of electron's incident waves ψ^{in} relate with the amplitudes in the hG-TMD ribbon ψ^{mid} through the matrix $D_{y=0}$.

$$\psi^{in} = D_{y=0}\psi^{mid}. \tag{3.7}$$

In matrix form, Eq.3.7 takes the following form.

$$\begin{bmatrix} 1 \\ 0 \\ r_1 \\ r_2 \end{bmatrix} = \begin{bmatrix} \beta(A_1 + B_1 e^{i\phi}) & \beta(A_2 + B_2 e^{i\phi}) & \beta(A_3 + B_3 e^{i\phi}) & \beta(A_4 + B_4 e^{i\phi}) \\ C_1 + D_1 e^{i\phi} & C_2 + D_2 e^{i\phi} & C_3 + D_3 e^{i\phi} & C_4 + D_4 e^{i\phi} \\ \alpha(A_1 - B_1 e^{-i\phi}) & \alpha(A_2 - B_2 e^{-i\phi}) & \alpha(A_3 - B_3 e^{-i\phi}) & \alpha(A_4 - B_4 e^{-i\phi}) \\ \gamma(C_1 - D_1) & \gamma(C_1 - D_1) & \gamma(C_1 - D_1) & \gamma(C_1 - D_1) \end{bmatrix} \begin{bmatrix} a_1 \\ a_2 \\ b_1 \\ b_2 \end{bmatrix}. \tag{3.8}$$

with $\beta = \sqrt{2}/(1 + e^{2i\phi})$, $\alpha = \sqrt{2}/(1 + e^{-2i\phi})$ and $\gamma = \sqrt{2}/(1 + e^{-i\phi})$. Analogously, from the second boundary condition $\psi_{II}(x, y = L) = \psi_{III}(x, y = L)$, the amplitudes of electron's transmitted waves ψ^{out} relate with the amplitudes in the hG-TMD ribbon ψ^{mid} through the matrix $D_{y=L}$.

$$\psi^{out} = D_{y=L}\psi^{mid}. \tag{3.9}$$

Matrix form of Eq. 3.9 is the following form

$$\begin{bmatrix} t_1 \\ t_2 \\ 0 \\ 0 \end{bmatrix} = \begin{bmatrix} \epsilon(A_1 + B_1) e^{i(q_{1y} - k_y)L} & \epsilon(A_2 + B_2) e^{i(q_{2y} - k_y)L} & \epsilon(A_3 + B_3) e^{i(q_{3y} - k_y)L} & \epsilon(A_4 + B_4) e^{i(q_{4y} - k_y)L} \\ \epsilon(C_1 + D_1) e^{i(q_{1y} - k_y)L} & \epsilon(C_2 + D_2) e^{i(q_{2y} - k_y)L} & \epsilon(C_3 + D_3) e^{i(q_{3y} - k_y)L} & \epsilon(C_4 + D_4) e^{i(q_{4y} - k_y)L} \\ (A_1 - B_1 e^{-i\phi}) e^{iq_{1y}L} & (A_2 - B_2 e^{-i\phi}) e^{iq_{2y}L} & (A_3 - B_3 e^{-i\phi}) e^{iq_{3y}L} & (A_4 - B_4 e^{-i\phi}) e^{iq_{4y}L} \\ (C_1 - D_1 e^{-i\phi}) e^{iq_{1y}L} & (C_2 - D_2 e^{-i\phi}) e^{iq_{2y}L} & (C_3 - D_3 e^{-i\phi}) e^{iq_{3y}L} & (C_4 - D_4 e^{-i\phi}) e^{iq_{4y}L} \end{bmatrix} \begin{bmatrix} a_1 \\ a_2 \\ b_1 \\ b_2 \end{bmatrix}. \tag{3.10}$$

with $\epsilon = \sqrt{2}/(1 + e^{i\phi})$.

From the Eq. 3.8 ψ^{mid} is obtained in terms of the inverse of $D_{y=0}$ and the amplitudes of electron's incident wave ψ^{in}. With this in mind, Eq. 3.9 is re-written as follows:

$$\psi^{out} = D_{(y0\to L)}\psi^{in}. \tag{3.11}$$

where $D_{(y0\to L)} = D_{y=L}{D_{y=0}}^{-1}$ is the transfer matrix of the ribbon structure and allows us to describe the electron's wave propagation in terms of coming ψ^{in} and outgoing waves ψ^{out}. This means that there is no need to explicitly establish the values of coefficients (a_i,b_i) inside the hG-TMD ribbon, although they can be obtained if needed.

3.2 Transport result in hG-TMD with no applied magnetic field

In this section, we will analyze transmission and reflection probabilities for the regimes of weak and strong SOC. For each case, we consider how these probabilities depend on kinetic energy and ribbon's width. In the first place, we keep the ribbon's width as a parameter ($L = 110nm$), the kinetic energy (ΔE) as the independent variable and the probabilities as the dependent variables. In the second place, ΔE is the parameter and L the variable modified in order to know its effect on probabilities.

As an example, we can see in figure 3.3 how the electron kinetic energy is determined for the regime of weak SOC. ΔE is given by the difference between the incident energy (E_i) and the minimal energy in the band (E_0). We consider fully propagating states in the hG-TMD region, $\Delta E > 0$.

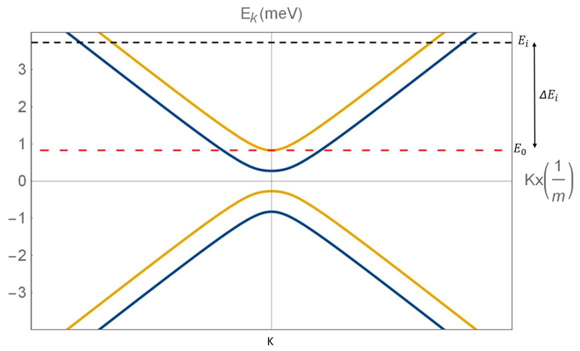

Figure 3.3: Representation of kinetic energy ΔE_i in terms of the incident energy (black dashed line) and minimal energy (red dashed line) in the energy band structure for $|S_1 + S_2| < \Delta$.

a.1) Strong SOC for constant hG-TMD ribbon width

Here we consider the *spin inverted band* regime (see figure 2.2). In this case $E_0 = 1.67meV$, and the electron incident energy takes three values: $E_1 = 2.67meV$, $E_2 = 4.67meV$ and $E_3 = 6.67meV$. Thus, three different kinetic energies for a constant width $L = 110nm$ are obtained.

From figures 3.4a and 3.4b it is possible to observe that the maximum $T_{\uparrow,\uparrow}$ and minimum $R_{\uparrow,\uparrow}$, are obtained for normal electron incidence for all ΔE, which means that at

$\phi = 0$ the electron does not seem to be affected by the TMD and its strong SOC. Besides, $T_{\uparrow,\uparrow}$ and $R_{\uparrow,\uparrow}$ probabilities are complementary.

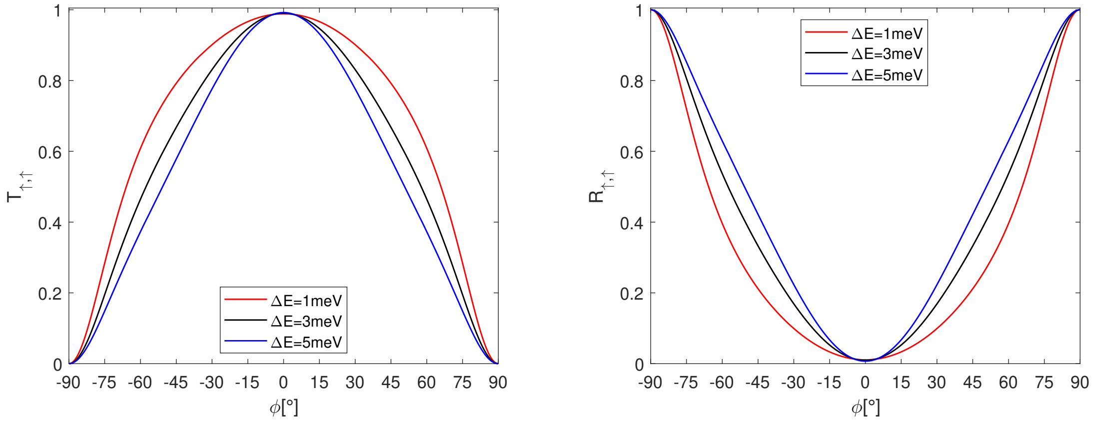

(a) $T_{\uparrow,\uparrow}$ (b) $R_{\uparrow,\uparrow}$

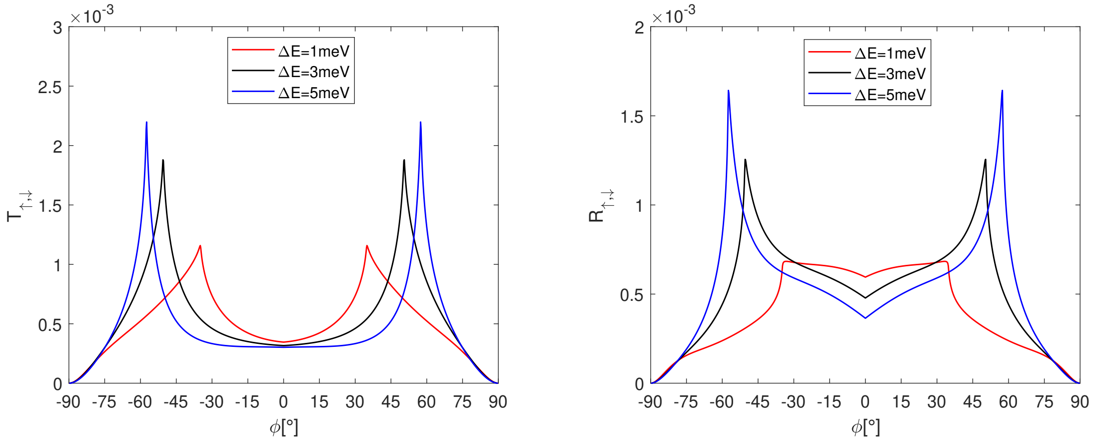

(c) $T_{\uparrow,\downarrow}$ (d) $R_{\uparrow,\downarrow}$

Figure 3.4: Probabilities of transmission and reflection for the regime of strong SOC. Kinetic energy varies from $1meV$ to $5meV$ and width is constant ($L = 110nm$). a) Spin-up to spin-up transmission, b) spin-up to spin-up reflection, c) spin-up to spin-down transmission and d) spin-up to spin-down reflection.

Additionally, the width of the $T_{\uparrow,\uparrow}$ normal incedence peak decreases as ΔE increases. Thus, the increment of kinetic energy allows the electron to increase in turn its probability of being transmitted or reflected with a modified spin (figures 3.4c and 3.4d). These probabilities are higher as the ΔE increases, which can be seen more clearly for

$\phi \approx 60^o$ and $\Delta E = 5meV$. Nonetheless, these probabilities are still very small even when they reach their maximum ($\approx 2 * 10^{-3}$).

a.2) Strong SOC for constant kinetic energy

Now the width of the hG-TMD ribbon changes and takes the values $50nm, 110nm, 400nm$ and $800nm$. $\Delta E = 3meV$ is kept constant, such that $E_0 = 1.67meV$ and $E_i = E_2 = 4.67meV$.

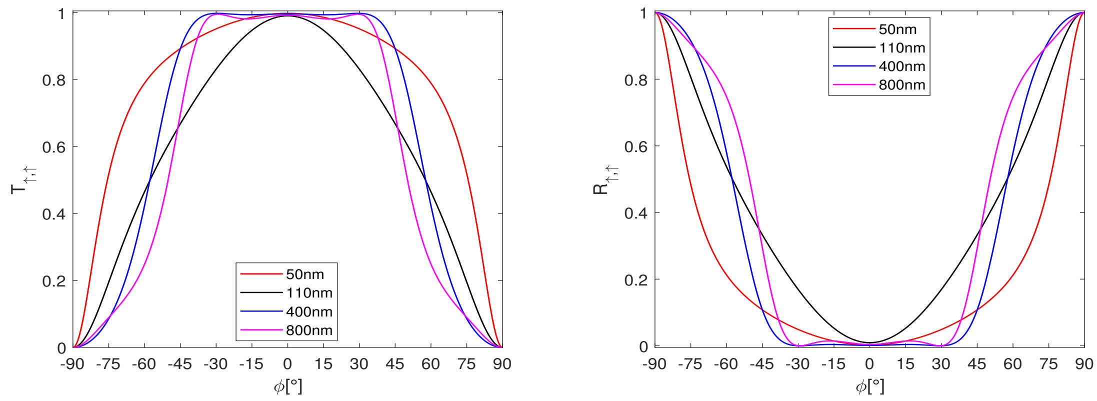

(a) $T_{\uparrow,\uparrow}$ (b) $R_{\uparrow,\uparrow}$

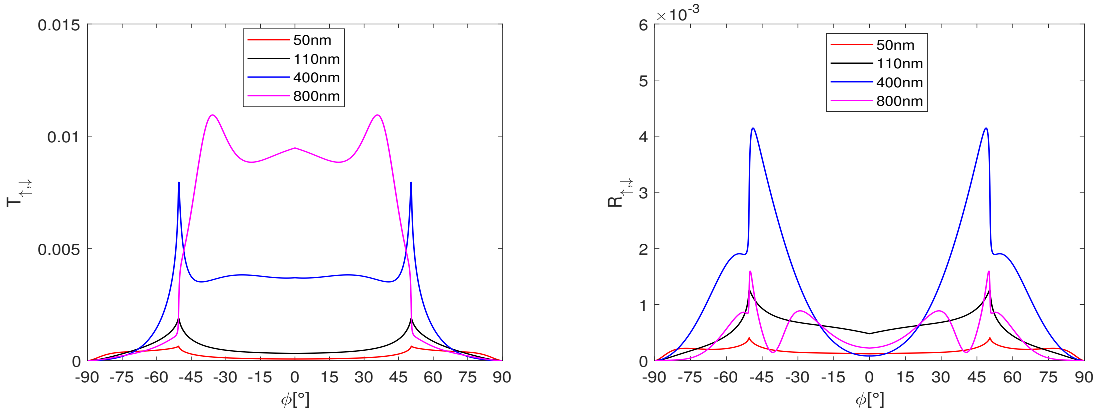

(c) $T_{\uparrow,\downarrow}$ (d) $R_{\uparrow,\downarrow}$

Figure 3.5: Probabilities of transmission and reflection for the regime of strong SOC. The hG-TMD ribbon width varies from $50nm$ to $800nm$ and kinetic energy is constant ($\Delta E = 3meV$). a) Spin-up to spin-up transmission, b) spin-up to spin-up reflection, c) spin-up to spin-down transmission and d) spin-up to spin-down reflection.

According to figure 3.5a, the width of the probability $T_{\uparrow,\uparrow}$ curve decreases as hG-TMD ribbon width increases, which implies that the electron probabilities with opposite spin enhance. Notice also the central peak gets flatter for larger width. Besides, it is possible to see that for spin flipping a small resonance arises when $L = 400nm$, and becomes more notorious for $L = 800nm$ and $\phi \approx \pm 50^o$.

As a consequence of the above exposed, $T_{\uparrow,\downarrow}$ increases significantly (an order of magnitude) for $L = 400nm$ and $L = 800nm$. Also, this probability reaches its maximum value for $L = 800nm$ and $\phi \approx \pm 38^o$ (see figure 3.5c). On the other hand, $R_{\uparrow,\downarrow}$ (figure 3.5d) maintains a similar order of magnitude than the previous-discussed case of constant width. Therefore, it is possible to say that the probability of an electron be transmitted or reflected with spin flipped is almost null for $L = 50nm$ and $L = 110nm$. Then, as the resonances starts to show up ($L = 800nm$), TMD affects the spin of electrons in graphene more intensely.

b.1) Weak SOC for constant hG-TMD ribbon width

In this case, the system is in the *direct band gap* regime (see figure 2.4) for $|S_1 + S_2| < \Delta$. Now $E_0 = 0.83meV$ and the electron's incident energy takes three values: $E_1 = 1.83meV$, $E_2 = 3.83meV$ and $E_3 = 5.83meV$, for a constant width $L = 110nm$.

In comparison with figure 3.5a, figure 3.6a exhibits transmission curves with wider peaks. Specifically, when $\Delta E = 1meV$ the coefficient $T_{\uparrow,\uparrow}$ is nearly 1 for a large range of ϕ values. Thus, the probability of the electron to be spin-flipped transmitted or reflected for this case is very small.

As the kinetic energy increases, the width of $T_{\uparrow,\uparrow}$ and $R_{\uparrow,\uparrow}$ diminishes. Particularly, for those angles at which $T_{\uparrow,\uparrow}$ decays rapidly ($60^o < \phi < 75^o$), $T_{\uparrow,\downarrow}$ and $R_{\uparrow,\downarrow}$ increases up to 0.011 and 0.009, respectively (see figures 3.6c and 3.6d). This behavior is comparable to the case $|S_1 + S_2| > \Delta$ for $L = 800nm$. Therefore, it is highlighted that in this regime, $|S_1 + S_2| < \Delta$, the probability of flipping the electron's spin is enhanced. Thus, when the electron moves along the system and the hG-TMD ribbon is in the *direct band gap* regime, the probabilities $T_{\uparrow,\downarrow}$ and $R_{\uparrow,\downarrow}$ reach the higher values allowed by the intrinsic SOC S_1, S_2, Rashba R and staggered potential Δ.

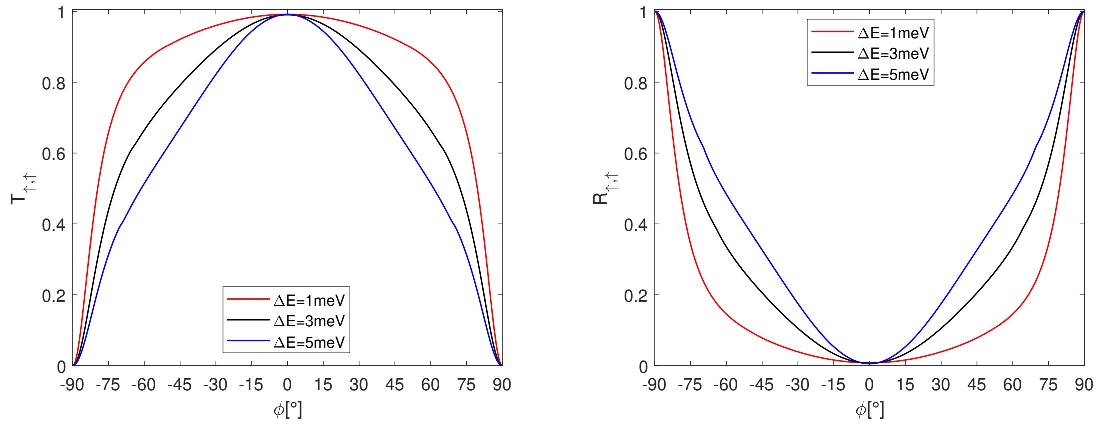

(a) $T_{\uparrow,\uparrow}$ (b) $R_{\uparrow,\uparrow}$

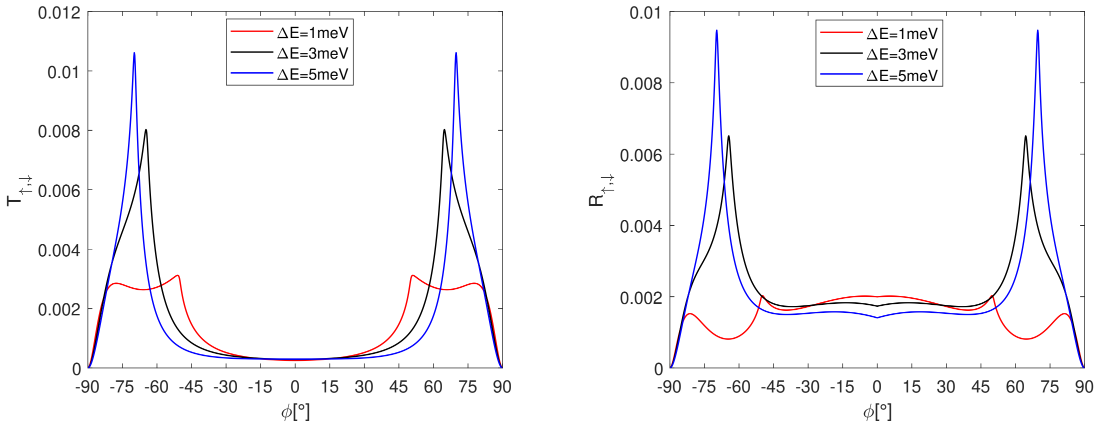

(c) $T_{\uparrow,\downarrow}$ (d) $R_{\uparrow,\downarrow}$

Figure 3.6: Probabilities of transmission and reflection for the regime of weak SOC. Kinetic energy varies from $1meV$ to $5meV$ and width is constant ($L = 110nm$). a) Spin-up to spin-up transmission, b) spin-up to spin-up reflection, c) spin-up to spin-down transmission and d) spin-up to spin-down reflection.

b.2) Weak SOC for constant kinetic energy

The probabilities $T_{\uparrow,\uparrow}$, $R_{\uparrow,\uparrow}$, $T_{\uparrow,\downarrow}$ and $R_{\uparrow,\downarrow}$ are obtained in this regime for different width hG-TMD ribbons, that is $L = 50nm, L = 110nm, L = 400nm$ and $L = 800nm$, and a constant kinetic energy of $3meV$ ($E_0 = 0.83meV$ and $E_i = E_2 = 3.83meV$).

According to figure 3.7a -and 3.7b-, $T_{\uparrow,\uparrow}$ decreases as L increases. Here resonances appear for $L = 800nm$, indeed in a more notorious way than in figure 3.5a for the hG-TMD affects more intensely the spin of electrons in graphene along a larger distance. Considering all the above mentioned, the probabilities $T_{\uparrow,\downarrow}$ and $R_{\uparrow,\downarrow}$ in this regime enhance for all L, especially for $L = 800nm$, which is possible to see in figures 3.7c and 3.7d. $T_{\uparrow,\downarrow}$ and $R_{\uparrow,\downarrow}$ reach values up to 0.035 and 0.027, respectively, for $\phi \approx 65^o$.

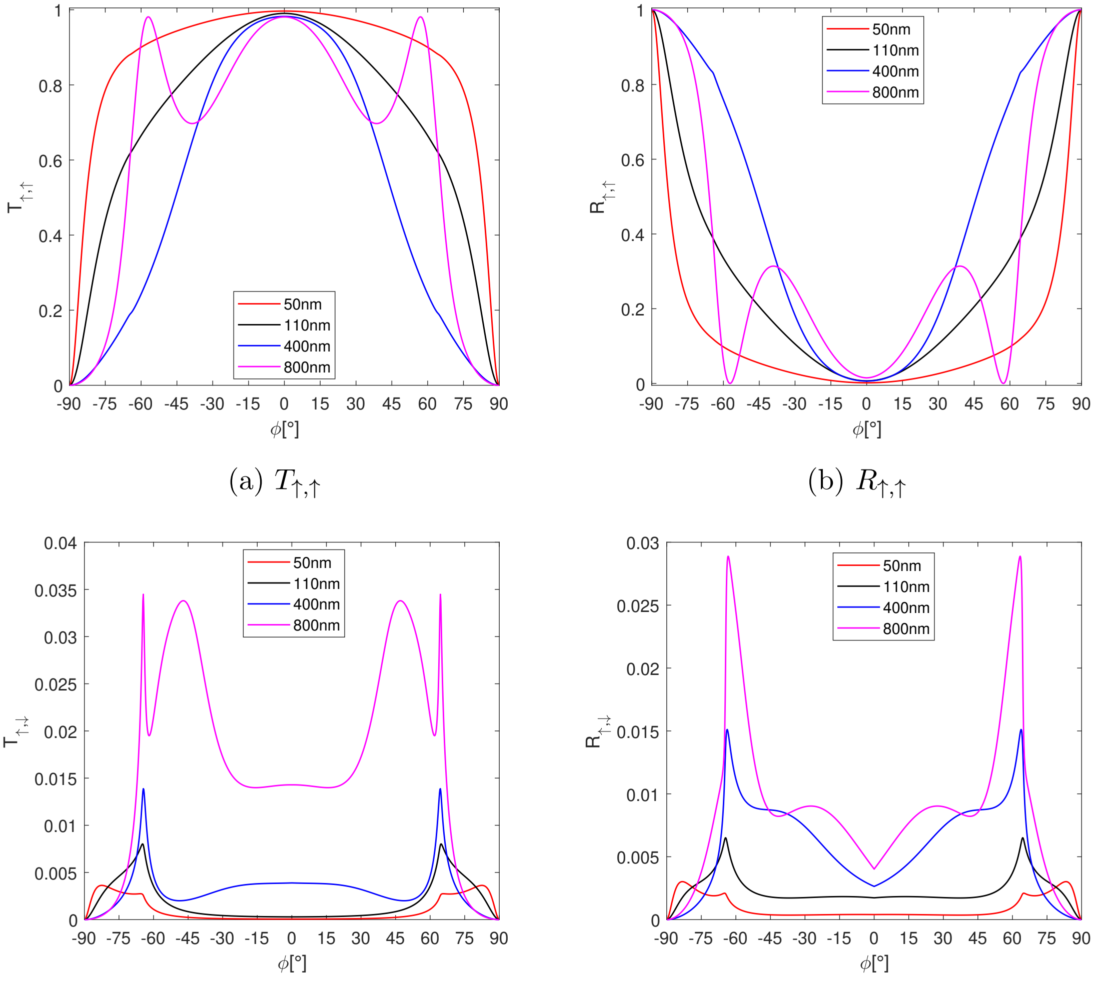

(a) $T_{\uparrow,\uparrow}$

(b) $R_{\uparrow,\uparrow}$

(c) $T_{\uparrow,\downarrow}$

(d) $R_{\uparrow,\downarrow}$

Figure 3.7: Probabilities of transmission and reflection for weak SOC regime. hG-TMD ribbon width varies from $50nm$ to $800nm$ and kinetic energy is constant ($\Delta E = 3meV$). a) Spin-up to spin-up transmission, b) spin-up to spin-up reflection, c) spin-up to spin-down transmission and d) spin-up to spin-down reflection.

As discussed before, this regime is the optimum in order to achieve an enhancement of transmission and reflection probabilities with spin flip. Indeed, these probabilities are higher in the weak SOC regime than in the strong one, for whatever chosen value of L and ΔE. This could be understood as follows: in the *direct bandgap* regime, bands have definite spin states; while *inverted band* regime, bands show spin states of different orientation (as we saw in *Chapter 2*) [2].

To briefly recap this section, we found that in the *inverted band* regime the best way to enhance $T_{\uparrow,\downarrow}$ and $R_{\uparrow,\downarrow}$ is increasing the hG-TMD ribbon width, for a constant kinetic energy. These probabilities reach their maximum values for $L = 800nm$, at the same time that resonances appear in $T_{\uparrow,\uparrow}$ and $R_{\uparrow,\uparrow}$. Additionally, it turns out that the probability of an electron to be transmitted or reflected with a flipped spin is higher in the weak SOC regime than in the strong SOC one, for any value of L and ΔE. The maximum values of $T_{\uparrow,\downarrow}$ and $R_{\uparrow,\downarrow}$ were reached for $L = 800nm$ in the weak SOC regime. In the end, the most optimum way to affect more effectively the spin of electrons in graphene is increasing the width of the hG-TMD ribbon, instead of augmenting the electron's incident energy.

3.3 Transport in hG-TMD under a magnetic field along the plane

We will discuss transmission and reflection probabilities for the weak and strong SOC regimes when a magnetic field is applied along the x direction [1]. Thus, it will establish the probabilities' dependence on magnetic field strength, kinetic energy, and ribbon's width. Firstly, the magnetic field varies from $4T$ to $40T$ while kinetic energy ($\Delta E = 3meV$) and ribbon's width ($L = 110nm$) are held constants. Secondly, the kinetic energy is modified ($\Delta E = 1meV, 3meV, 5meV$) for constant values of the magnetic field ($B = 40T$) and ribbon's width ($L = 110nm$).

a.1) Strong SOC for constant hG-TMD ribbon width and kinetic energy

To study the system under these conditions, we consider a magnetic field of $4T$, with electron incident energy $E_i = E_2 = 4.69meV$ and the minimal energy $E_0 = 1.69meV$. For $B = 20T$, $E_2 = 5.15meV$ and $E_0 = 2.15meV$, while for $B = 40T$, $E_2 = 6.10meV$ and

---

[1] The transmission and reflection probabilities for the weak and strong SOC regimes when a magnetic field is applied along y direction are similar to those along the x one. These probabilities are presented in *Apendix 3*.

$E_0 = 3.10meV$.[2] All these values are taken in order to keep $\Delta E = 3meV$ and $L = 110nm$ as fixed parameters.

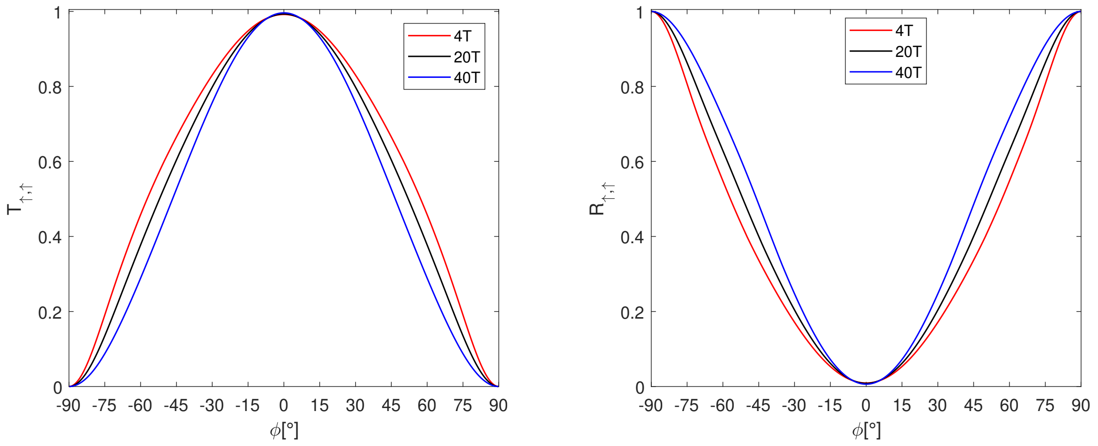

(a) $T_{\uparrow,\uparrow}$ (b) $R_{\uparrow,\uparrow}$

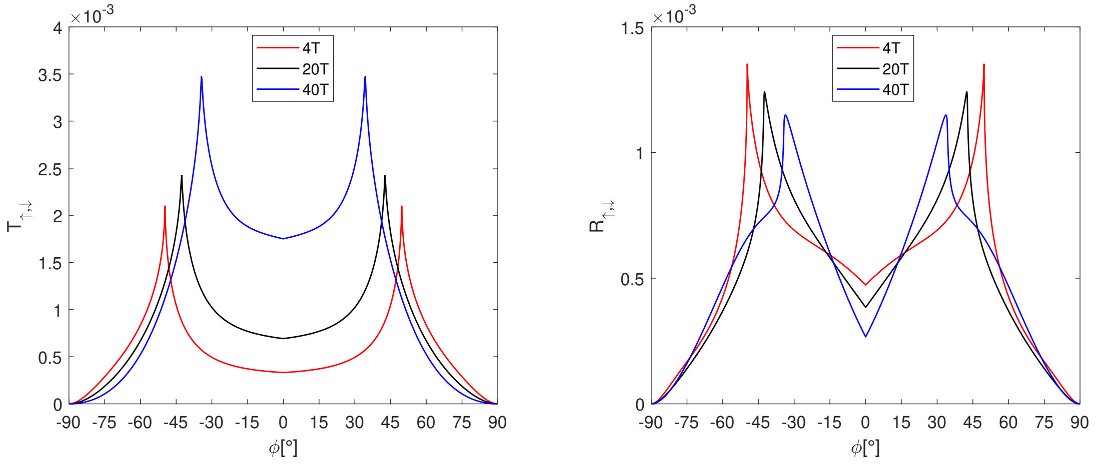

(c) $T_{\uparrow,\downarrow}$ (d) $R_{\uparrow,\downarrow}$

Figure 3.8: Probabilities of transmission and reflection for the regime of strong SOC. B varies from $4T$ to $40T$ while kinetic energy and L are constants ($\Delta E = 3meV; L = 110nm$). a) Spin-up to spin-up transmission, b) spin-up to spin-up reflection, c) spin-up to spin-down transmission and d) spin-up to spin-down reflection.

From figures 3.8a and 3.8b, it is seen that the peak widths of $T_{\uparrow,\uparrow}$ and $R_{\uparrow,\uparrow}$ decrease as the magnetic field increases. It is worth noting that these changes are small, which allows

---

[2] See figure 3.3 to understand the notation for E_0 and E_2

us to expect that the changes in $T_{\uparrow,\downarrow}$ and $R_{\uparrow,\downarrow}$ also would be small, as effectively happens (see figures 3.8c and 3.8d).

$T_{\uparrow,\downarrow}$ reaches its maximum value for $B = 40T$ and $\phi \approx \pm 35^o$. It is worth noting that comparing the $T_{\uparrow,\downarrow}$ behavior under the action of magnetic fields, to the absence of them, see figure 3.4, for the same ΔE and L, an enhancement of this probability is observed for all values of magnetic field.

On the other hand, $R_{\uparrow,\downarrow}$ is maximum for $B = 4T$ and $\phi \approx \pm 57^o$. However, $R_{\uparrow,\downarrow}$, under the action of magnetic fields, does not vary so much in comparison to those values obtained in figure 3.4d when $B = 0$, same energy and ribbon width. Thus, the presence of the magnetic field on the enhancement of this probability is hardly noticeable.

a.2) Strong SOC for constant hG-TMD ribbon width and magnetic field

The magnetic field $B = 40T$ and $L = 110nm$ are now the fixed parameters. For a minimal energy of $E_0 = 3.1meV$ and electron's incident energies $E_1 = 4.1meV$, $E_2 = 6.1meV$ and $E_3 = 8.19meV$, kinetic energy varies from $1meV$ to $5meV$.

Under the action of a strong magnetic field, both $T_{\uparrow,\uparrow}$ and $R_{\uparrow,\uparrow}$ almost overlap for higher kinetic energies ($\Delta E = 3meV$ and $\Delta E = 5meV$). This behavior is different to that we found for $B = 0$ as shown in figure 3.4a.

Comparing to those values obtained in figures 3.4c and 3.4d, the probabilities $T_{\uparrow,\downarrow}$ and $R_{\uparrow,\downarrow}$ (see figures 3.9c and 3.9d) are enhanced when the magnetic field is turned on. In fact, these probabilities increase as the kinetic energy does. Also, their maximum values shift from $\phi = 0^o$ as soon as the energy increases. In conclusion, under a strong magnetic field and with high kinetic energy, the electron increases the probabilities of being transmitted or reflected with spin-flip.

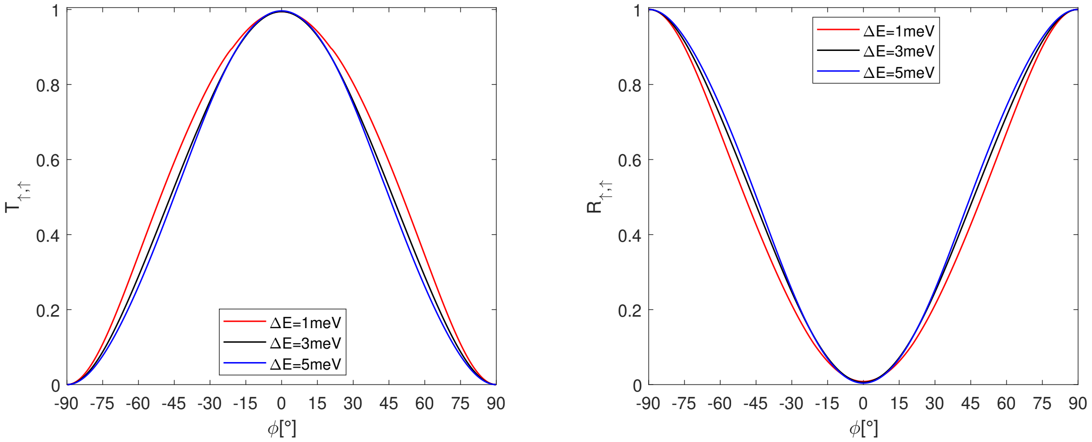

(a) $T_{\uparrow,\uparrow}$ (b) $R_{\uparrow,\uparrow}$

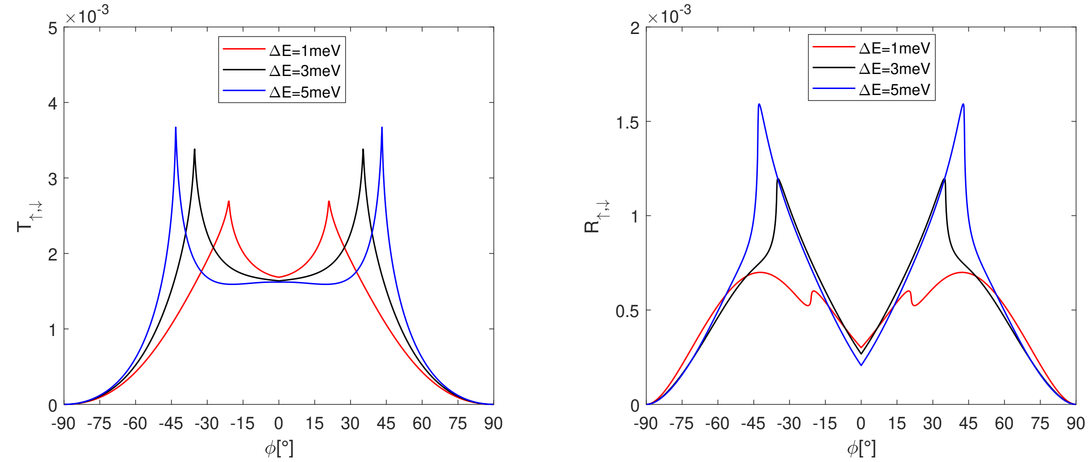

(c) $T_{\uparrow,\downarrow}$ (d) $R_{\uparrow,\downarrow}$

Figure 3.9: Probabilities of transmission and reflection for the regime of strong SOC. ΔE varies from $1meV$ to $5meV$ while B and L are constants ($B = 40T; L = 110nm$). a) Spin-up to spin-up transmission, b) spin-up to spin-up reflection, c) spin-up to spin-down transmission and d) spin-up to spin-down reflection.

b.1) Weak SOC for constant hG-TMD ribbon width and kinetic energy

We consider a magnetic field of $4T$, the electron incident energy $E_i = E_2 = 3.9meV$ and the minimal energy $E_0 = 0.9meV$. For $B = 20T$, $E_2 = 4.71meV$, for $E_0 = 1.71meV$; and for $B = 40T$, $E_2 = 5.85meV$ and $E_0 = 2.85meV$. All these values are selected in order to keep $\Delta E = 3meV$ and $L = 110nm$ as fixed parameters.

As observed in figures 3.10a and 3.10b, the peak widths of $T_{\uparrow,\uparrow}$ and $R_{\uparrow,\uparrow}$ decrease as the magnetic field increases. In the regime of *direct bandgap*, the difference between the curves as the magnetic field increases is more notorious that in the *inverted band* regime (see figures 3.8a and 3.8b).This means that the differences between $T_{\uparrow,\downarrow}$ -also $R_{\uparrow,\downarrow}$- curves for each magnetic field are going to be larger in the first regime than in the second one.

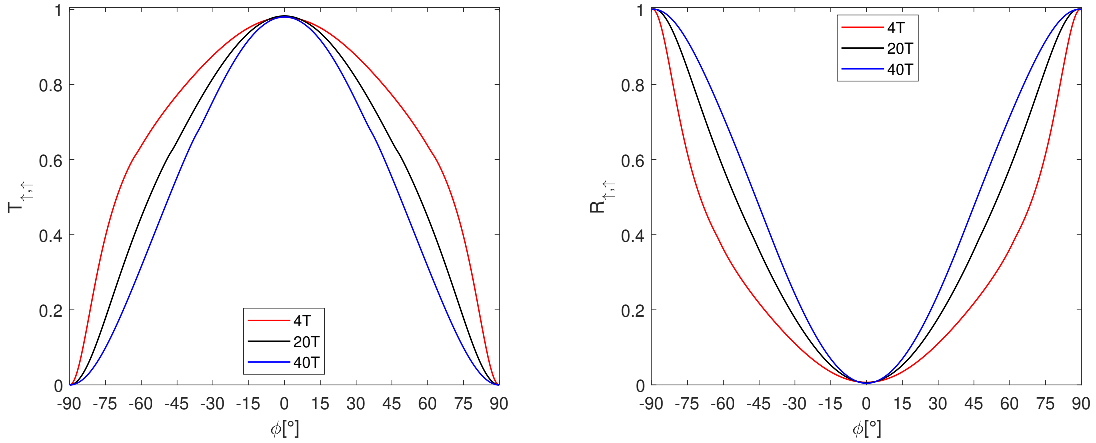

(a) $T_{\uparrow,\uparrow}$ (b) $R_{\uparrow,\uparrow}$

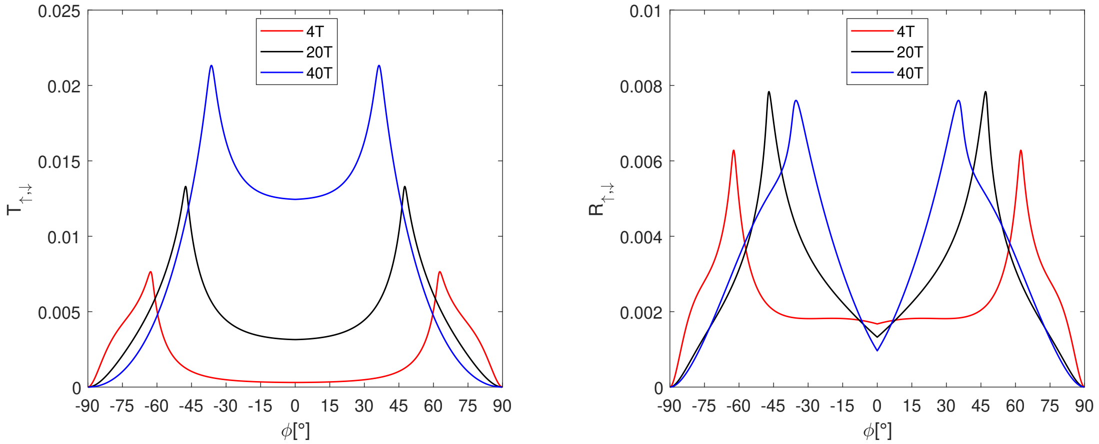

(c) $T_{\uparrow,\downarrow}$ (d) $R_{\uparrow,\downarrow}$

Figure 3.10: Probabilities of transmission and reflection for the regime of weak SOC. B varies from $4T$ to $40T$ while kinetic energy and L are constants ($\Delta E = 3meV; L = 110nm$). a) Spin-up to spin-up transmission, b) spin-up to spin-up reflection, c) spin-up to spin-down transmission and d) spin-up to spin-down reflection.

The maximum value of $T_{\uparrow,\downarrow}$ is reached for $B = 40T$ and $\phi \approx \pm 35^o$. It is worth noting that comparing the $T_{\uparrow,\downarrow}$ behavior under the action of magnetic fields, with the case of figure 3.6c, when $B = 0$, $\Delta E = 3meV$ and $L = 110nm$ (black line), an enhancement of this probability is obtained for all values of magnetic field. Indeed the spin-flip transmission transits from $T_{\uparrow,\downarrow} \approx 8 * 10^{-3}$ without B, to values up to $T_{\uparrow,\downarrow} \approx 2.2 * 10^{-2}$ with $B = 40T$ (see figure 3.10c).

On the other hand, $R_{\uparrow,\downarrow}$ is maximum for $B = 20T$ and $\phi \approx \pm 57^o$. Under the action of magnetic fields, $R_{\uparrow,\downarrow}$ varies from $\approx 6.5 * 10^{-3}$ to $\approx 8 * 10^{-3}$, a comparable enhancement to those obtained in figure 3.6d for a null field.

In the *direct bandgap* regime, the spin states become strongly polarized as the magnetic field becomes stronger. This explains why the probability that an electron be transmitted and reflected with the opposite spin in the hG-TMD under the action of B is the highest achieved until now.

b.2) Weak SOC for constant hG-TMD ribbon width and magnetic field

The magnetic field $B = 40$ and $L = 110nm$ are held constant. In order to vary the kinetic energy from $1meV$ to $5meV$, the minimal energy is $E_0 = 2.85meV$ and electron's incident energies are $E_1 = 3.85meV$, $E_2 = 5.85meV$ and $E_3 = 7.85meV$.

Comparing figure 3.6a (3.6b) to 3.11a (3.11b) it is noticed that once the magnetic field is turned on, $T_{\uparrow,\uparrow}$ ($R_{\uparrow,\uparrow}$) is very similar for all values of kinetic energy.

The probabilities $T_{\uparrow,\downarrow}$ and $R_{\uparrow,\downarrow}$ (see figures 3.11c and 3.11d) are enhanced when the magnetic field is turned on. In fact, these probabilities also increase as the kinetic energy does. Thus, when the hG-TMD is under the action of a strong magnetic field and the electron has a high kinetic energy, the probabilities of being transmitted or reflected flipping its spin are enhanced in comparison to those values obtained in figures 3.6c and 3.6d.

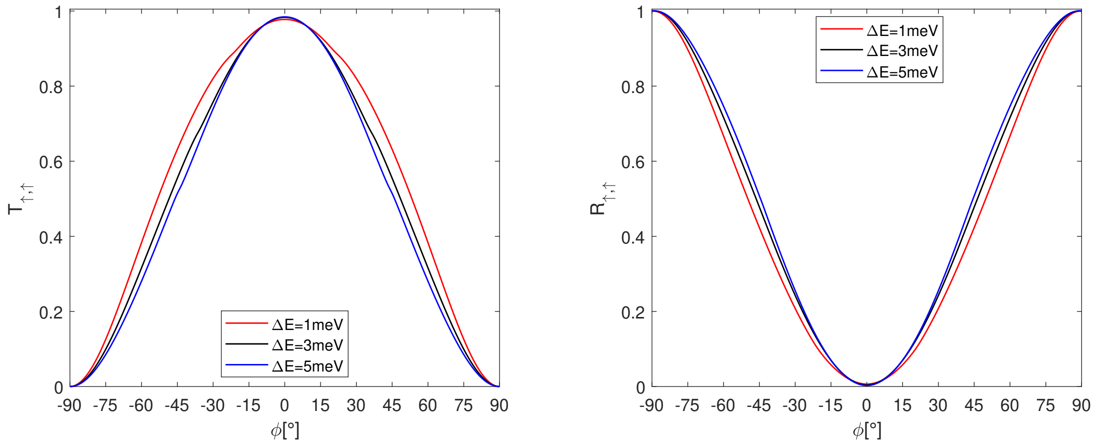

(a) $T_{\uparrow,\uparrow}$ (b) $R_{\uparrow,\uparrow}$

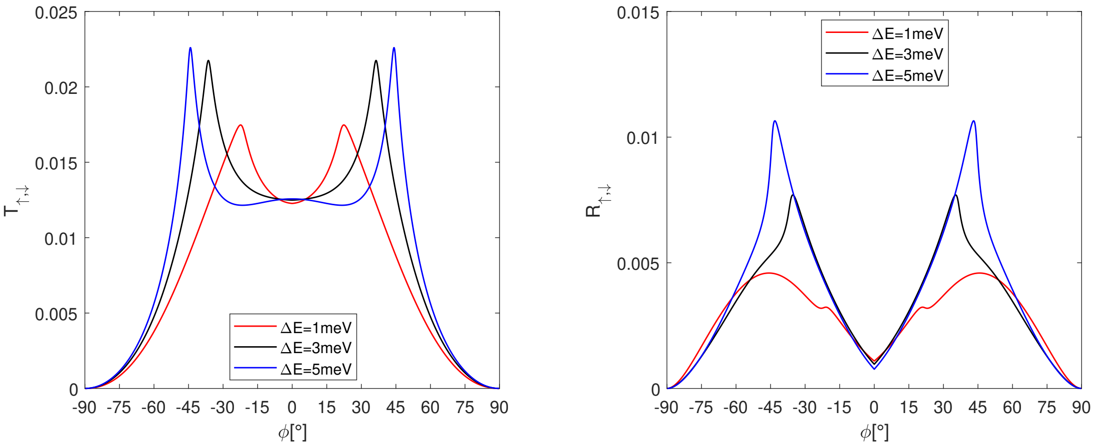

(c) $T_{\uparrow,\downarrow}$ (d) $R_{\uparrow,\downarrow}$

Figure 3.11: Probabilities of transmission and reflection for the regime of weak SOC. ΔE varies from $1meV$ to $5meV$ while B and L are constants ($B = 40T; L = 110nm$). a) Spin-up to spin-up transmission, b) spin-up to spin-up reflection, c) spin-up to spin-down transmission and d) spin-up to spin-down reflection.

Taking into account the above discussed, we conclude that the *direct bandgap* regime, when a strong magnetic field is applied, is the optimum in order to achieve an enhancement of $T_{\uparrow,\downarrow}$ and $R_{\uparrow,\downarrow}$. Therefore, the ribbon width of the hG-TMD will be changed just for this case. The probabilities $T_{\uparrow,\uparrow}$, $R_{\uparrow,\uparrow}$, $T_{\uparrow,\downarrow}$ and $R_{\uparrow,\downarrow}$ are then obtained for $L = 50, 110, 400$ and $800nm$. Kinetic energy and magnetic field are kept as fixed parameters

($\Delta E = 3meV$, which means $E_0 = 2.85meV$ and $E_2 = 5.85meV$; $B = 40T$).

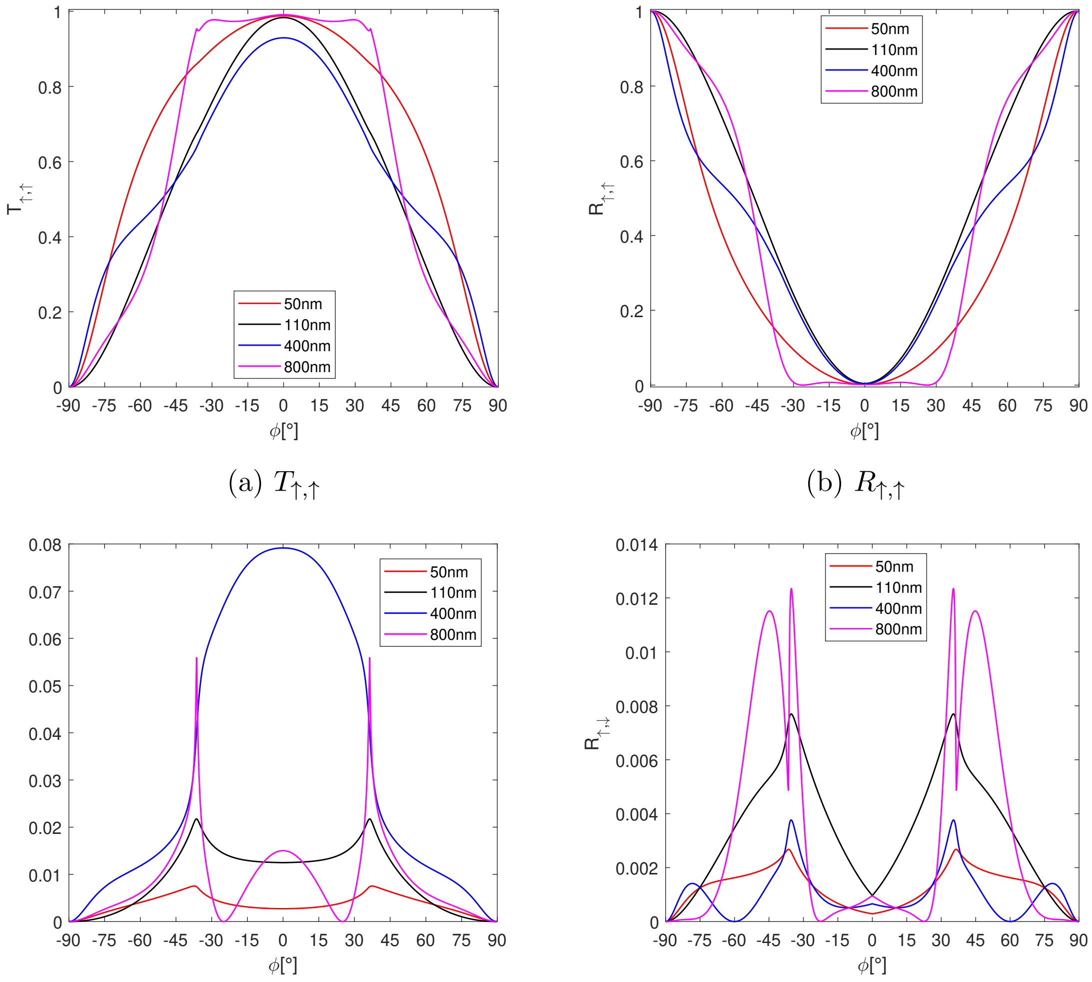

(a) $T_{\uparrow,\uparrow}$ (b) $R_{\uparrow,\uparrow}$

(c) $T_{\uparrow,\downarrow}$ (d) $R_{\uparrow,\downarrow}$

Figure 3.12: Probabilities of transmission and reflection for the regime of weak SOC. hG-TMD ribbon width varies from $50nm$ to $800nm$, while kinetic energy and magnetic field are constant ($\Delta E = 3meV; B = 40T$). a) Spin-up to spin-up transmission, b) spin-up to spin-up reflection, c) spin-up to spin-down transmission and d) spin-up to spin-down reflection

According to figure 3.12a, $T_{\uparrow,\uparrow}$ decreases as L increases for $L = 50$ and $L = 110nm$. This behavior changes for the case $L = 400nm$ and $\phi = \pm 45^o$. Besides, resonances appear for $L = 800nm$, although in a less notorious way than in figure 3.7a

Due to the fact that $T_{\uparrow,\uparrow}$ for $L = 400nm$ reaches its highest values not of 1 but 0.92, $T_{\uparrow,\downarrow}$ is especially enhanced up to 0.08 (see figure 3.12c). It is highlighted that for all values of L, this latter probability is significantly higher than the obtained for the case without magnetic field. Besides, $R_{\uparrow,\downarrow}$ is enhanced for all L, as seen in figure 3.7d.

To finalize, our results show that in the *direct bandgap* and *inverted band* regimes, the probability of an electron being transmitted or reflected, once it passes through the ribbon of hG-TMD, is enhanced for both directions x or y of the magnetic field. In fact, all $T_{\uparrow,\uparrow}$, $T_{\uparrow,\uparrow}$, $T_{\uparrow,\downarrow}$ and $R_{\uparrow,\downarrow}$ are similar for both directions of the field in the different explored cases.

Additionally, we found in the *strong SOC* regime that $T_{\uparrow,\downarrow}$ and $R_{\uparrow,\downarrow}$ are enhanced when the magnetic field and the kinetic energy take their higher values. In the *weak SOC* regime the probability of an electron being transmitted or reflected with opposite spin is higher than in the *strong SOC* one. Besides, these probabilities increase even more if the hG-TMD ribbon is wider ($L = 400nm$ and $L = 800nm$). Thus, the best way to modify the spin of electrons in the proposed nanostructure is by increasing the applied magnetic field and the width of the hG-TMD ribbon in the *direct bandgap* regime, for a constant kinetic energy, because the polarization of spin states becomes higher for strong magnetic fields.

Chapter 4

Conclusions

The study of hG-TMD through the effective Hamiltonian model allows us to find two regimes in the energy band structure of this system: a) the *inverted band* regime ($\mid S_1 + S_2 \mid > \Delta$), which shows both spin states in the bands near to the K point and b) the *direct bandgap* regime ($\mid S_1 + S_2 \mid < \Delta$), whose bands show definite spin states. In the first regime, the SOC terms are strong to compete with the staggered potential Δ, which causes the spin (S_z) to change its projection along z axis, around the Dirac point. In the second situation, the S_z does not change direction because SOC is not strong enough to compete with Δ. In both cases, all spin textures display circular contours, which means that the energy band structures and spin textures are radially symmetric around the K point.

When a magnetic field is applied along the x or y direction, the symmetries of the energy band structure and the spin texture are preserved along the direction of the magnetic field applied, otherwise, they are broken.

In the situation of weak field, the magnetic field is $4T$, the spin behavior for both regimes is analogous to that obtained in the case of $B = 0$. Nonetheless, when the applied magnetic field gets intense ($40T$), spin projection along z direction changes for both situations: in the *strong SOC* regime, the magnitude of S_z is significantly reduced because the spin couples to the intense field, aligning its direction along the xy plane, while in the *weak SOC* one, a mini-inverted-spin band is created. Therefore, the manipulation of spin is allowed in the system by choosing the appropriate parameter values.

Additionally, for a magnetic field perpendicular to hG-TMD, the eigenstates can be found analytically. Thus, the eigenvectors of the system are described in terms of parabolic cylinder functions, and the eigenenergies depend on a discrete value p. When the Rashba term is zero, pure spin states and spin-degenerate Landau levels are obtained, otherwise Rashba interaction gives rise to spin mixing.

When analyzing the electronic transport in a system composed of pristine graphene and a ribbon of hG-TMD, we found that the probability of an electron to be transmitted or reflected with spin flip is higher in the *weak SOC* regime than in the *strong SOC* regime, for any value of ribbon width of hG-TMD and kinetic energy. This behavior could be explained because of the definite spin states of the bands in the *direct bandgap* case. The maximum values of $T_{\uparrow,\downarrow}$ and $R_{\uparrow,\downarrow}$ are reached for $L = 800nm$, as the resonances appear in $T_{\uparrow,\uparrow}$ and $R_{\uparrow,\uparrow}$. Thus, from this perspective, the optimal way to affect more intensely the spin of electrons in graphene is increasing the width of the hG-TMD ribbon, and not increasing the electron's incident energy.

In the case that the above described system is under the action of an applied magnetic field along the x or y direction, no matter its magnitude, the transmission and reflection probabilities associated to electron are similar in both situations, which means that electron transport does not distinguish between these directions of B.

Furthermore, as soon as the magnetic field increases, $T_{\uparrow,\downarrow}$ and $R_{\uparrow,\downarrow}$ are enhanced, whatever regime, compared to the $B = 0$ case. However, it is remarkable that the best option to enhance these probabilities is found in the *Weak SOC* regime, as we brought up earlier.

With this in mind, the probability of an electron being transmitted or reflected with the opposite spin is enhanced by increasing the applied magnetic field and the width of the hG-TMD ribbon, which could be understood because the polarization of spin states becomes stronger in the *direct bandgap* regime, for a constant kinetic energy.

Having examined the behavior of the energy band structure, spin textures, and transport when graphene is in proximity to TMD and under the action of applied magnetic fields in different directions, it is important to point out further options that can be studied in the future. Firstly, the number of hG-TMD ribbons in the system could be increased, keeping constant or varying the width of these ribbons. Another possibility, might be to analyze the electronic transport when the heterostructure is affected by a magnetic field with both in-plane and out-of-plane components. Also, in order to explore how to increase the spin-flip, the Rashba term could be changed. Finally, we could go deeper and calculate the density current in this system. All these perspectives yield to a better understanding of the spin manipulation in two-dimensional structures and their possible applications.

Appendix A

Solution for the perpendicular magnetic field

The vector potential that corresponds to **B**=B$\hat{\mathbf{z}}$ is given by the Eq. 2.10, thus H_{eff} is influenced by the interaction between the magnetic field and the spin. Particularly, just the Hamiltonian of pristine graphene, which is the only term of H_{eff} that depends on momentum (see Eq. 1.6), assumes the following form:

$$H_0 = v_f(\tau_z s_0 \sigma_x (p_x + \frac{e}{c}(-By)) + \tau_0 s_0 \sigma_y p_y), \tag{A.1}$$

since the vector potential depends on y, the momentum $p_x = \hbar k_x$ is a conserved quantity, while $p_y = i\hbar\partial_y$ does not. Thus, the effective Hamiltonian eigenstates preserve the translational invariance along x-direction. In addition, it has to be considered that along the y direction the system is piecewise constant (this can be seen in Eq. 2.12).

Taking into account Eqs. 2.7 and 2.5 we can write the Zeeman interaction Hamiltonian for this case as follows:

$$H_{Zeeman}{}^{K} = \mu_B B \begin{bmatrix} 1 & 0 & 0 & 0 \\ 0 & 1 & 0 & 0 \\ 0 & 0 & -1 & 0 \\ 0 & 0 & 0 & -1 \end{bmatrix}. \tag{A.2}$$

Thus, we can write the total Hamiltonian of the systems as in the Eq: 2.11.

Moreover, with the definition of dimensionless quantities given in Eqs. 2.13, 2.14

and 2.16 it is possible to solve the Eq. 2.17 through the following process:

$$\begin{bmatrix} \nu_- & a & 0 & 0 \\ a^\dagger & \nu_+ & i\lambda & 0 \\ 0 & -i\lambda & \mu_+ & a \\ 0 & 0 & a^\dagger & \mu_- \end{bmatrix} \begin{bmatrix} \phi_1 \\ \phi_2 \\ \phi_3 \\ \phi_4 \end{bmatrix} = 0. \tag{A.3}$$

where $\phi_1 \equiv \phi_{A\uparrow K}$, $\phi_2 \equiv \phi_{B\uparrow K}$, $\phi_1 \equiv \phi_{A\downarrow K}$ and $\phi_1 \equiv \phi_{B\downarrow K}$. From this expression we obtain:

$$\begin{aligned} \phi_1 &= -\frac{a\phi_2}{\nu_-}, \\ a^\dagger\phi_1 + \nu_+\phi_2 + i\lambda\phi_3 &= 0, \\ -i\lambda\phi_2 + \mu_+\phi_3 + a\phi_4 &= 0, \\ \phi_4 &= -\frac{a^\dagger\phi_3}{\mu_-}. \end{aligned} \tag{A.4}$$

Reeplacing the first and fourth equations in the second and third ones, we have:

$$\begin{aligned} \phi_3 &= \frac{a^\dagger a - \nu}{i\lambda\nu_-}\phi_2, \\ i\lambda\mu_-\phi_2 + (a^\dagger a + 1 - \mu)\phi_3 &= 0 \\ &. \end{aligned} \tag{A.5}$$

Combining these two expressions and multiplying by $i\lambda\nu_-$:

$$\begin{aligned} [(a^\dagger a + 1 - \mu)(a^\dagger a - \nu) - \lambda^2\mu_-\nu_-]\phi_2 &= 0, \\ \mathcal{D}\phi_2 &= 0. \end{aligned} \tag{A.6}$$

This $\mathcal{D}$ operator commutes with $a^\dagger a$:

$$\begin{aligned} [\mathcal{D}, a^\dagger a] = [(a^\dagger a)^n + c, a^\dagger a] &= [(a^\dagger a)^n, a^\dagger a] + [c, a^\dagger a], \\ [\mathcal{D}, a^\dagger a] &= ((a^\dagger a)^n a^\dagger a - a^\dagger a(a^\dagger a)^n) = 0. \end{aligned}$$

hence ϕ_2 is an eigenstate of $a^\dagger a$. Thereby,

$$(a^\dagger a)\phi_2 = p\phi_2 \tag{A.7}$$

where p is an eigenvalue. From this perspective and taking into account Eq. A.6, we find the eigenvalues equation:

$$(p+1-\mu)(p-\nu) = \lambda^2 \mu_- \nu_- . \tag{A.8}$$

From Eq. A.7 and using the definitions in Eq. 2.16, we have that:

$$a^\dagger a = aa^\dagger - 1 = (\frac{\eta}{2} + \partial_\eta)(\frac{\eta}{2} - \partial_\eta) - 1.$$

$$a^\dagger a = (\frac{\eta}{2})^2 - \partial_\eta^2 - \frac{\eta}{2}\partial_\eta + \partial_\eta \frac{\eta}{2} - 1.$$

with $\partial_\eta = \frac{d}{d\eta}$ and $\partial_\eta \frac{\eta}{2} = \frac{1}{2} + \frac{\eta}{2}\partial_\eta$. Therefore:

$$(p - a^\dagger a)\phi_2(\eta) = 0,$$

$$(\frac{d^2}{d\eta^2} + p + \frac{1}{2} - \frac{\eta^2}{4})\phi_2(\eta) = 0 \tag{A.9}$$

which is the differential equation of the parabolic cylinder functions [18]. This equation has four linearly independent solutions given by: $D_p(\eta), D_p(-\eta), D_{-p-1}(i\eta), D_{-p-1}(-i\eta)$. We will only use the first two; to build the spinor ϕ_η, as they are the only ones who are normalizable.

Accordingly to the above-mentioned, we can write ϕ_2 in terms of these parabolic cylindrical functions and find the other components with the help of Eqs. A.4 and A.5. We will also need the following recurrence relations [18]:

$$\begin{aligned} aD_p(\eta) &= pD_{p-1}(\eta), \\ a^\dagger D_p(\eta) &= D_{p+1}(\eta), \\ aD_p(-\eta) &= -pD_{p-1}(-\eta), \\ a^\dagger D_p(-\eta) &= -D_{p+1}(-\eta). \end{aligned} \tag{A.10}$$

With this set of equations, the following eigenvectors are obtained:

$$\phi_p = \begin{pmatrix} -pD_{p-1}(\eta) \\ \nu_- D_p(\eta) \\ i\frac{\nu-p}{\lambda} D_p(\eta) \\ -i\frac{\nu-p}{\mu_-\lambda} D_{p+1}(\eta) \end{pmatrix}, \begin{pmatrix} pD_{p-1}(-\eta) \\ \nu_- D_p(-\eta) \\ i\frac{\nu-p}{\lambda} D_p(-\eta) \\ i\frac{\nu-p}{\mu_-\lambda} D_{p+1}(-\eta) \end{pmatrix}. \tag{A.11}$$

From Eq. A.8, we obtain:

$$p^2 - (\mu + \nu - 1)p - \nu(1 - \mu) = \lambda^2 \mu_- \nu_-.$$

With the definitions given in Eq. 2.20 and reorganizing terms:

$$\begin{aligned} p^2 - p[(E + b + S_2)^2 - (S_1 - \Delta)^2 - 1] + \\ [(E - b - S_2)^2 - (S_1 + \Delta)^2]\{[1 - (E + b + S_2)^2 - (S_1 - \Delta)^2] - p\} = \\ \lambda^2[(E - S_1)^2 - (b + S_2 + \Delta)^2]. \end{aligned}$$

Finally, we get the equation for the energy in terms of p:

$$\begin{aligned} [(E + b + S_2)^2 - (p + 1 + (S_1 - \Delta)^2)] + \\ [(E - b - S_2)^2 - (p + (S_1 + \Delta)^2)] = \\ \lambda^2[(E - S_1)^2 - (b + S_2 + \Delta)^2]. \end{aligned} \tag{A.12}$$

Appendix B

hG-TMD under a magnetic field along y direction

In this case the magnetic field is applied along $\hat{\mathbf{y}}$. We will present the most representative two cases, when $\mid S_1 + S_2 \mid > \Delta$ for B=4T, and when $\mid S_1 + S_2 \mid < \Delta$ for B=40T. The two other remaining cases, when $\mid S_1 + S_2 \mid > \Delta$ for B=40T, and when $\mid S_1 + S_2 \mid < \Delta$ for B=4T can be easily understood taking into account the corresponding section in *Chapter two*. In the first case, spin band inversion is also present (see figure 2.9), and in the second one, the magnetic field strength is not enough to produce a change in the energy band structure (see figure 2.12) and pure texture spin (see figures 2.13 and 2.14).

a) Strong SOC and weak magnetic field

The magnetic field is weak (4T), then the energy band structures do not change much from those we have seen in figure 2.2. However, it is important to point out that the symmetry along k_x is not preserved, while in k_y it is, as observed in B.1a.

The magnetic field along y direction also affects the spin texture, which is more evident if we separately analyze the cross sections. In this sense, we can see that B.2b is identical to 2.7a, which means that the symmetry is kept along the direction of the applied magnetic field. The same is valid for B.1b and 2.6a.

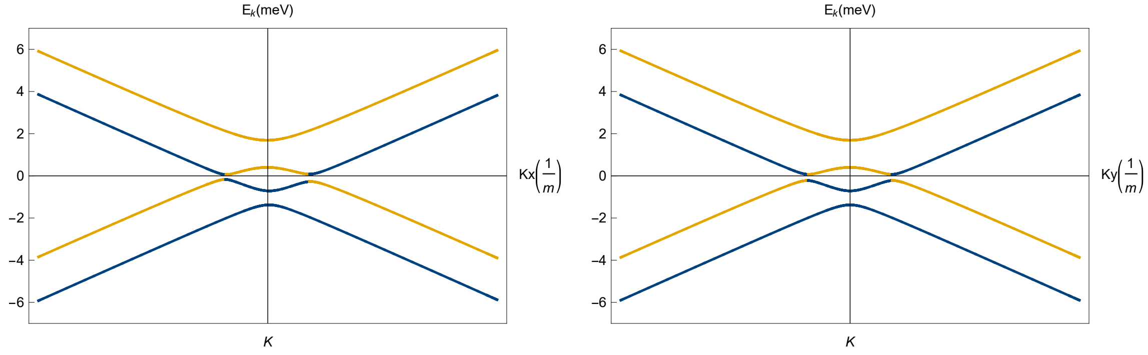

(a) $E(k_x)$ (b) $E(k_y)$

Figure B.1: Band structure in the regime of *inverted band* when $|S_1+S_2| > \Delta$ and magnetic energy $\approx 0.23meV$. a) Band structure for $k_y = 0$. b) Band structure for $k_x = 0$.

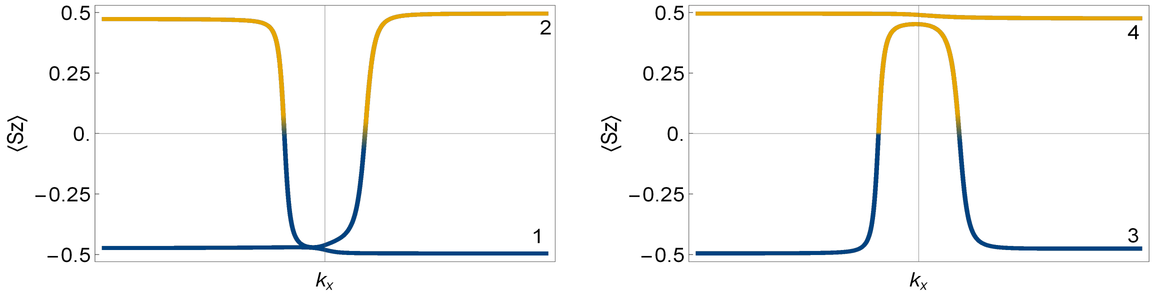

(a) $S_z(k_x)$

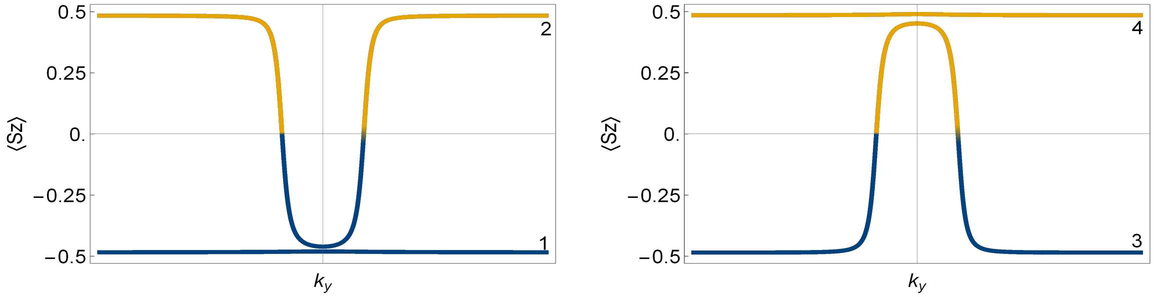

(b) $S_z(k_y)$

Figure B.2: Cross sections of spin projection along z axis in the regime of high SOC with a magnetic energy of $\approx 0.23meV$. These sections show a broken symmetry along the k_x direction. a) Spin texture for $k_y = 0$. b) Spin texture for $k_x = 0$.

In figure B.2 the upper (lower) row shows S_z as a function of k_x (k_y). The symmetry of these textures does not remain (remain) along k_x (k_y). Therefore, in the spin texture (figure B.3) this asymmetry is highlighted because the contours are not concentric.

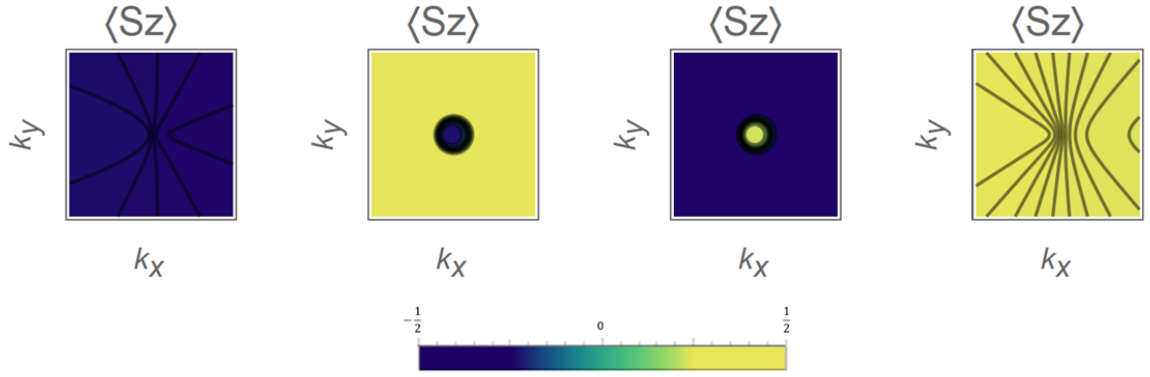

Figure B.3: Spin texture when $B = 4T$ and $|S_1 + S_2| > \Delta$. Taking into account the second and third squares, it is possible to see that spin band inversion around K point exists for small magnetic fields.

b)Weak SOC and strong magnetic field

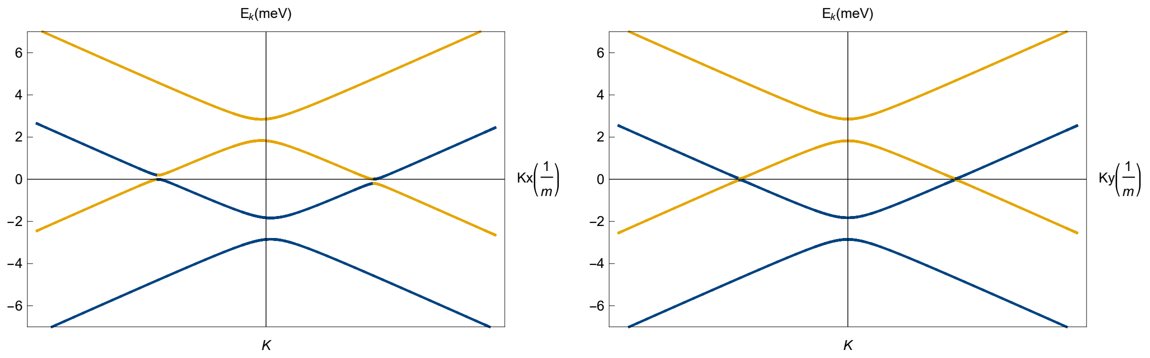

(a) $E(k_x)$ (b) $E(k_y)$

Figure B.4: Band structure in the regime of weak SOC when $|S_1 + S_2| < \Delta$ and magnetic energy $\approx 2.3meV$. a) Band structure for $k_y = 0$. b) Band structure for $k_x = 0$.

When the magnetic field increases,up to B=40T, it is possible to see how a slight spin band inversion is produced between the second and third band (figure B.4). Moreover, the symmetry of the band structure, as well as the spin, is still broken along k_x direction.

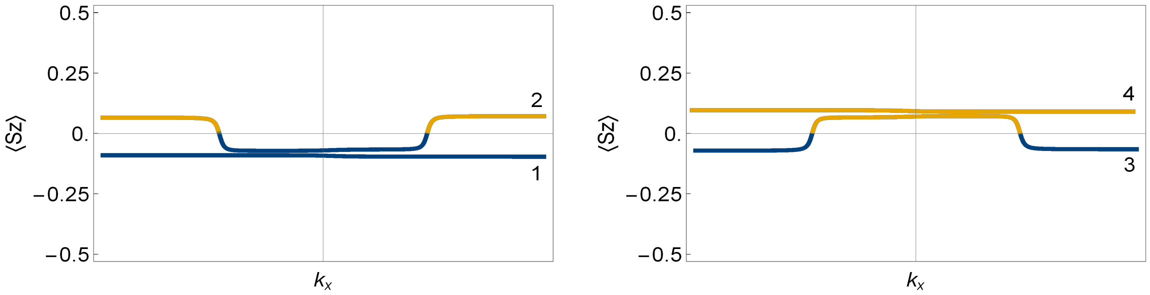

(a) $S_z(k_x)$

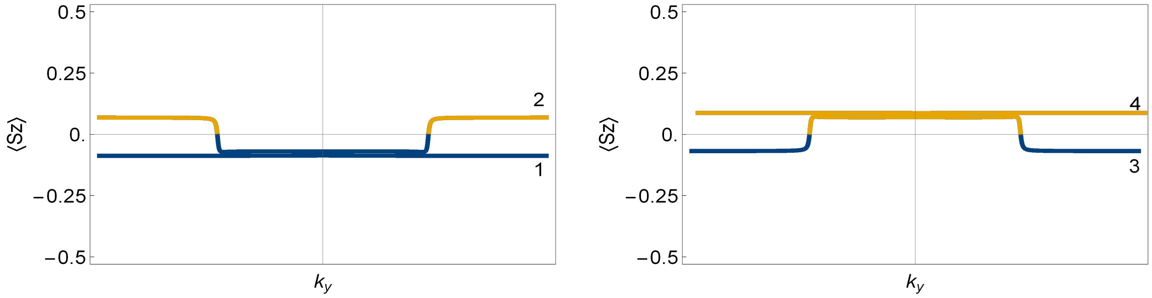

(b) $S_z(k_y)$

Figure B.5: Cross sections of spin projection along z axis in the regime of weak SOC with a magnetic energy of $\approx 2.3meV$. These sections show a broken symmetry along the k_x direction while it is symmetric along k_y. a) Spin texture for $k_y = 0$. b) Spin texture for $k_x = 0$.

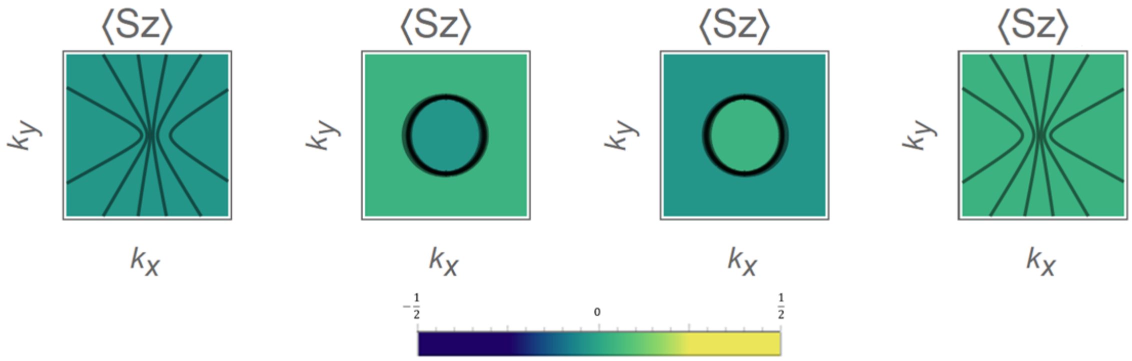

Figure B.6: Spin texture for $B = 40T$ and $|S_1 + S_2| < \Delta$. From Left to right, the first and fourth square shows defined negative and positive spin values, respectively. According to the second and third squares, a small spin inversion band has been created because of the magnetic field strength.

We found an inverted band when $|S_1 + S_2| < \Delta$ as is shown in the cross-section of spin texture in figure B.5. The first square represents the values of spin in the first (lowest) energy band of the band structure: spin is negative (its value is close to zero). The second square represents the change of spin from positive (nearly zero) to negative (also around Dirac point) in the second band. The third one changes from negative to positive. The last one is entirely positive.

In figure B.6 we can see that spin does not reach the possible minimal or maximal values. Hence, the color of the spin texture in figure oscillates from light blue to light green.

As we mentioned in *Chapter 2*, SOC and magnetic field-spin interaction energy compete.The increase of one of them can change the band structure and the behavior of spin in the graphene-TMD structure. The magnetic field strength has been enough in order to provoke a slight spin inversion band.

To summarize, the energy band structure and the spin texture changes along the perpendicular direction of the applied magnetic field. Then, symmetry is broken along the x-direction and remains on the y-axis.

Appendix C

Electron transport under a magnetic field along *y* direction

The probability of an electron being transmitted or reflected with spin-up or spin-down is presented for the case in which the magnetic field strength changes from $4T$ to $40T$, along $\hat{\mathbf{y}}$, keeping kinetic energy ($\Delta E = 3meV$) and ribbon width ($L = 110nm$) as constants. It is discussed for both cases: *inverted band* regime ($\mid S_1 + S_2 \mid > \Delta$) and *direct bandgap* regime ($\mid S_1 + S_2 \mid < \Delta$). The remaining cases, ΔE increasing up to $5mev$ for $L = 110nm$ and B as constants, and the ribbon width varying from $50nm$ to $800nm$ while ΔE and B are constants, are exactly the same as that for B along the x direction in the corresponding section in *Chapter 3*.

a.1) Strong SOC for constant hG-TMD ribbon width and kinetic energy

We analyze the behavior of the system for three field intensities. When the magnetic field is $4T$, the electron's incident energy $E_2 = 4.69meV$ and the minimal energy $E_0 = 1.69meV$; for $B = 20T$, $E_2 = 5.15meV$ and $E_0 = 2.1meV$; and for $B = 40T$, $E_2 = 6.10meV$ and $E_0 = 3.10meV$. Notice that for all these values $\Delta E = 3meV$ and $L = 110nm$ are fixed parameters.

The peak width of $T_{\uparrow,\uparrow}$ and $R_{\uparrow,\uparrow}$ decreases as the magnetic field increases from $4T$ to $40T$ (see figures C.1a and C.1b. The coefficient $T_{\uparrow,\downarrow}$ reaches its maximum value for $B = 40T$ and $\phi \approx \pm 35^o$. It is worth noting that comparing the $T_{\uparrow,\downarrow}$ behaviour under the action of magnetic fields, to the case of figure 3.4, $B = 0$, $\Delta E = 3meV$ and $L = 110nm$, an enhancement of this probability for all values of magnetic field is obtained. On the other hand, $R_{\uparrow,\downarrow}$ is maximum for $B = 4T$ and $\phi \approx \pm 57^o$. However, $R_{\uparrow,\downarrow}$, under the action of magnetic fields, does not vary so much in comparison to those values shown in figure 3.4d.

The behavior of these probabilities is exactly the same for both x and y directions of the applied magnetic field, as seen in figure 3.8.

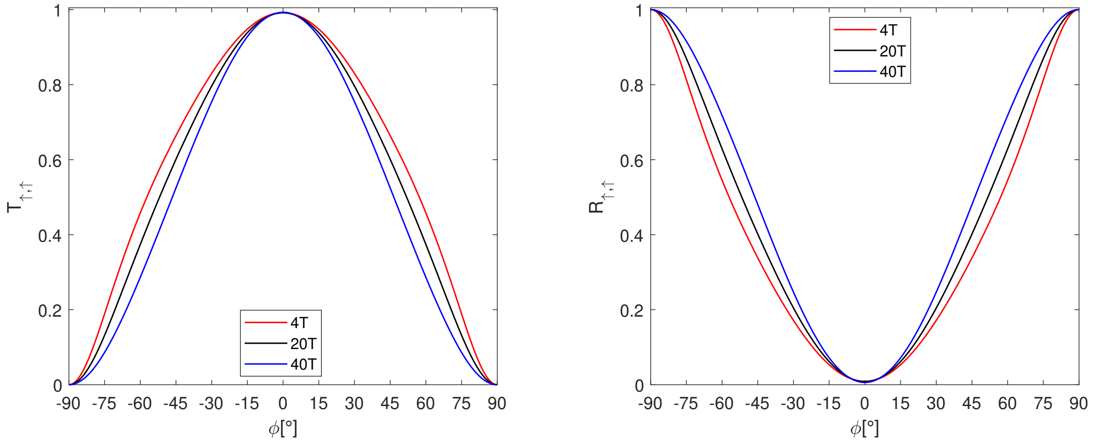

(a) $T_{\uparrow,\uparrow}$ (b) $R_{\uparrow,\uparrow}$

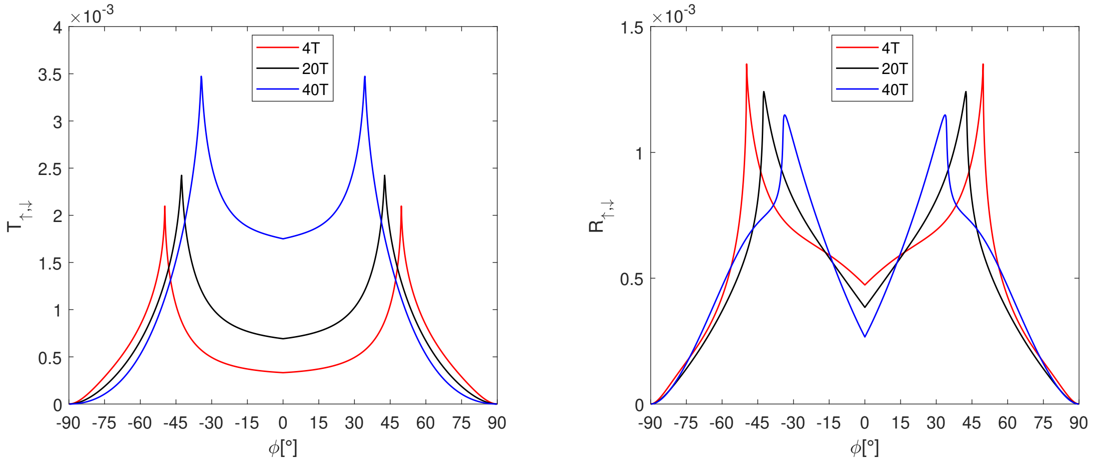

(c) $T_{\uparrow,\downarrow}$ (d) $R_{\uparrow,\downarrow}$

Figure C.1: Probabilities of transmission and reflection for the regime of strong SOC. B varies from $4T$ to $40T$ while kinetic energy and L are constants ($\Delta E = 3meV; L = 110nm$). a) Spin-up to spin-up transmission, b) spin-up to spin-up reflection, c) spin-up to spin-down transmission, and d) spin-up to spin-down reflection.

b.1) Weak SOC for constant hG-TMD ribbon width and kinetic energy

When the magnetic field is $4T$, the electron's incident energy $E_2 = 3.9meV$ and the minimal energy $E_0 = 0.9meV$; for $B = 20T$, $E_2 = 4.71meV$ and $E_0 = 1.71meV$; and for $B = 40T$, $E_2 = 5.85meV$ and $E_0 = 2.85meV$. $\Delta E = 3meV$ and $L = 110nm$ are parameters.

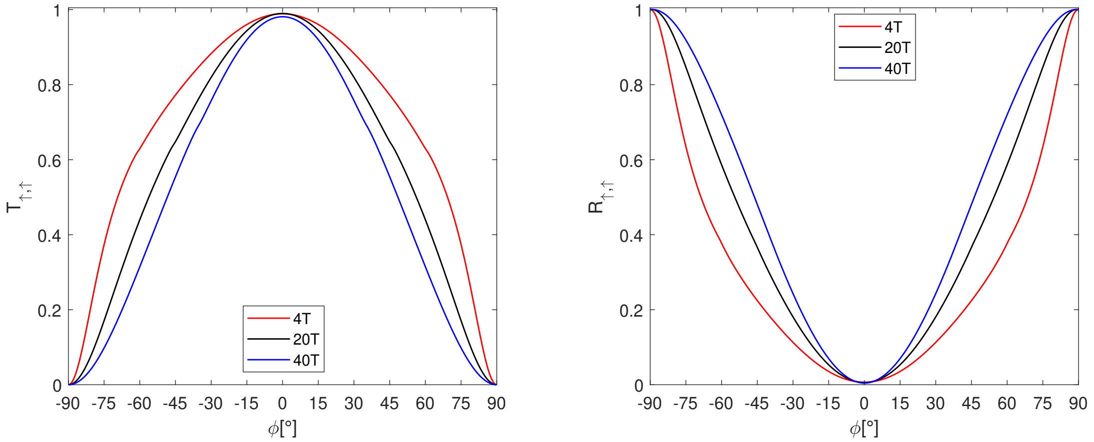

(a) $T_{\uparrow,\uparrow}$ (b) $R_{\uparrow,\uparrow}$

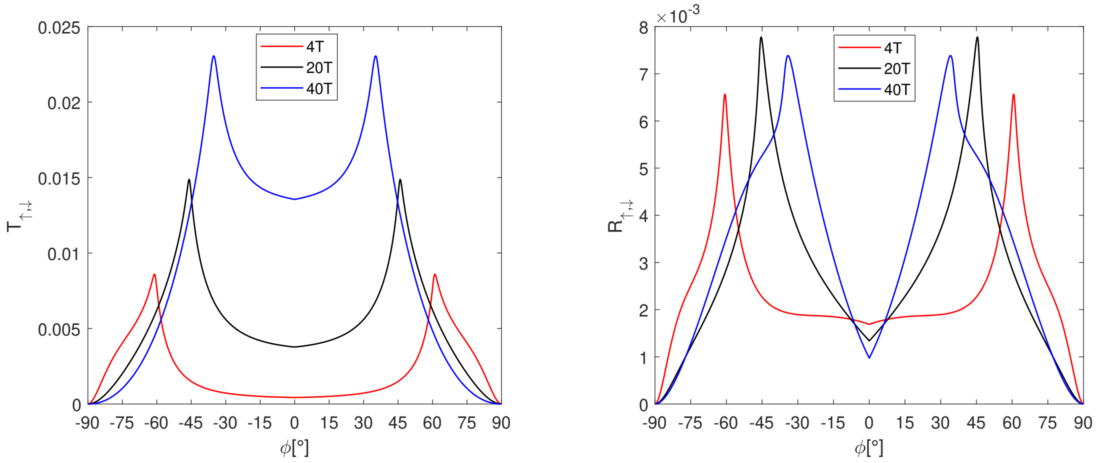

(c) $T_{\uparrow,\downarrow}$ (d) $R_{\uparrow,\downarrow}$

Figure C.2: Probabilities of transmission and reflection for the regime of weak SOC. B varies from $4T$ to $40T$ while kinetic energy and L are constants ($\Delta E = 3meV; L = 110nm$). a) Spin-up to spin-up transmission, b) spin-up to spin-up reflection, c) spin-up to spin-down transmission, and d) spin-up to spin-down reflection.

In the regime of *direct bandgap*, the difference between the $T_{\uparrow,\uparrow}$ curves as well as $R_{\uparrow,\uparrow}$, as the magnetic field augments is more notorious that in the *inverted band* regime (see figures C.2a and C.1a).

The maximum value of $T_{\uparrow,\downarrow}$ is reached for $B = 40T$ and $\phi \approx \pm 35^o$. It is worth noting that comparing the $T_{\uparrow,\downarrow}$ behaviour under the action of magnetic fields, to the case of figure 3.6c, where $B = 0$, $\Delta E = 3meV$ and $L = 110nm$ (black line), an enhancement of this probability for all values of magnetic field is obtained (see figure C.2c). Notice that $R_{\uparrow,\downarrow}$ is maximum for $B = 20T$ and $\phi \approx \pm 57^o$. Under the action of magnetic fields, $R_{\uparrow,\downarrow}$ augments comparing to those values obtained in figure 3.6d, where $B = 0$, $\Delta E = 3meV$ and $L = 110nm$.

As well as the above mentioned case, these probabilities behaves exactly the same no matters if the magnetic field is along x or y direction, which can be seen in figure 3.10.

To sum up, the electron transport is not affected by the direction of the magnetic field along the plane. Moreover, the *direct bandgap* regime shows the highest probability of that an electron transmitted or reflected with the opposite spin in the hG-TMD under the action of B.

Bibliography

[1] Novoselov, K. S., Andreeva, D. V., Ren, W., &. Shan, G. (2019). Graphene and other two-dimensional materials. Frontiers of Physics, 14(1), 13301.

[2] Singh, S., Alsharari, A.M., Ulloa, S.E. and Romero, A.H. (2019). Proximity-Induced Topological Transition and Strain-Induced Charge Transfer in Graphene/MoS2 Bilayer Heterostructures. In Handbook of Graphene Set (eds E. Celasco, A.N. Chaika, T. Stauber, M. Zhang, C. Ozkan, C. Ozkan, U. Ozkan, B. Palys and S.W. Harun). doi:10.1002/9781119468455.ch39.

[3] Geim, A. K., &. Grigorieva, I. V. (2013). Van der Waals heterostructures. Nature, 499(7459), 419-425.

[4] Ávalos-Ovando, O., Mastrogiuseppe, D., &. Ulloa, S. E. (2019). Lateral heterostructures and one-dimensional interfaces in 2D transition metal dichalcogenides. Journal of Physics: Condensed Matter, 31(21), 213001.

[5] Novoselov, K. S., Fal, V. I., Colombo, L., Gellert, P. R., Schwab, M. G., &. Kim, K. (2012). A roadmap for graphene. Nature, 490(7419), 192-200.

[6] Hulman, M. (2014). Raman spectroscopy of graphene. In Graphene (pp. 156-183). Woodhead Publishing.

[7] Neto, A. C., Guinea, F., Peres, N. M., Novoselov, K. S., &. Geim, A. K. (2009). The electronic properties of graphene. Reviews of Modern Physics, 81(1), 109.

[8] Choi, W., Choudhary, N., Han, G. H., Park, J., Akinwande, D., &. Lee, Y. H. (2017). Recent development of two-dimensional transition metal dichalcogenides and their applications. Materials Today, 20(3), 116-130.

[9] Wang, Z., Ki, D. K., Chen, H., Berger, H., MacDonald, A. H., &. Morpurgo, A. F. (2015). Strong interface-induced spin–orbit interaction in graphene on WS_2. Nature Communications, 6(1), 1-7.

[10] Kis, Andras. (2012). Graphene is not alone. Nat. Nanotechnol, 7, 683.

[11] Xiao, D., Liu, G. B., Feng, W., Xu, X., &. Yao, W. (2012). Coupled spin and valley physics in monolayers of MoS 2 and other group-VI dichalcogenides. Physical Review Letters, 108(19), 196802.

[12] Alsharari, A. M., Asmar, M. M., &. Ulloa, S. E. (2016). Mass inversion in graphene by proximity to dichalcogenide monolayer. Physical Review B, 94(24), 241106.

[13] Bercioux, D., &. De Martino, A. (2019). Spin-orbit interaction and snake states in a graphene pn junction. Physical Review B, 100(11), 115407.

[14] Avsar, A., Tan, J. Y., Taychatanapat, T., Balakrishnan, J., Koon, G. K. W., Yeo, Y., &. Eda, G. (2014). Spin–orbit proximity effect in graphene. Nature Communications, 5(1), 1-6.

[15] Island, J. O., Cui, X., Lewandowski, C., Khoo, J. Y., Spanton, E. M., Zhou, H., Rhodes, D., Hone, J. C., Taniguchi, T., Watanabe, K., Levitov, L. S., Zaletel, M. P., &. Young, A.F. (2019). Spin–orbit-driven band inversion in bilayer graphene by the van der Waals proximity effect. Nature, 571(7763), 85-89.

[16] Gmitra, M., &. Fabian, J. (2015). Graphene on transition-metal dichalcogenides: A platform for proximity spin-orbit physics and optospintronics. Physical Review B, 92(15), 155403.

[17] Kane, C. L., &. Mele, E. J. (2005). Quantum spin Hall effect in graphene. Physical Review Letters, 95(22), 226801.

[18] De Martino, A., Hütten, A., &. Egger, R. (2011). Landau levels, edge states, and strained magnetic waveguides in graphene monolayers with enhanced spin-orbit interaction. Physical Review B, 84(15), 155420.

[19] Markos, P., &. Soukoulis, C. M. (2008). Wave propagation: from electrons to photonic crystals and left-handed materials. Princeton University Press.